J. Fluid Mech. (2016), *vol.* 799, *pp.* 637–672.
doi:10.1017/jfm.2016.374

Experimental investigation of the water entry of a rectangular plate at high horizontal velocity

A. Iafrati†

CNR-INSEAN, Marine Technology Research Institute, Rome 00128, Italy

(Received 29 September 2015; revised 17 March 2016; accepted 27 May 2016;
first published online 28 June 2016)

The water entry of a rectangular plate with a high horizontal velocity component is investigated experimentally. The test conditions are representative of those encountered by aircraft during emergency landing on water and are given in terms of three main parameters: horizontal velocity, approach angle, i.e. vertical to horizontal velocity ratio, and pitch angle. Experimental data are presented in terms of pressure, spray root shape, pressure peak propagation velocity and total loads acting on the plate. A theoretical solution of the plate entry problem based on two-dimensional and potential flow assumptions is derived and is used to support the interpretation of the experimental measurements. The results indicate that, as the plate penetrates and the ratio between the plate breadth and the wetted length measured on the longitudinal plane diminishes, the role of the third dimension becomes dominant. The increased possibility for the liquid to escape from the lateral sides yields a reduction of the pressure peak propagation velocity and, consequently, of the corresponding pressure peak intensity. In particular, it is shown that, at the beginning of the entry process, the pressure peak moves much faster than the geometric intersection between the body and the free surface, but at a later stage the two points move along the body at the same speed. Furthermore, it is shown that the spray root develops a curved shape which is almost independent of the specific test conditions, even though the initial growth rate of the curvature is higher for larger pitch angles. The loads follow a linear increase versus time, as predicted by the theoretical model, only in a short initial stage. Next, for all test conditions examined here, they approach a square-root dependence on time. It is seen that, if the loads are scaled by the square of the velocity component normal to the plate, the data are almost independent of the test conditions.

Key words: flow–structure interactions, multiphase flow, waves/free-surface flows

1. Introduction

Water entry with horizontal speed is of interest in the naval field for problems related to the slamming of large-displacement ships (Kapsenberg 2011) and the unsteady pitching motion of high-speed planing craft (Stenius *et al.* 2013). The problem is also important in aeronautics: the emergency landing of aircraft on water (known as ditching) and its theoretical understanding are important aspects in

---

† Email address for correspondence: alessandro.iafrati@cnr.it

assessing aircraft safety. As a part of the design process, air-worthiness authorities ask aircraft manufacturers to analyse ditching in order to obtain certification of the airframe. The interest in ditching has motivated specific research activities in the past (Smiley 1950, 1951, 1952; Smith, Warren & Wright 1957) and more recently (Climent *et al.* 2006; Seddon & Moatamedi 2006; Streckwall, Lindenau & Bensch 2007; Zhang, Li & Dai 2012; Guo *et al.* 2013).

For the purposes of airframe design and certification, the use of computational approaches, although still at the development stage, is becoming technically feasible (Siemann & Groenenboom 2014; Siemann *et al.* 2014). Examples of numerical simulations of aircraft ditching are provided in Streckwall *et al.* (2007) and Guo *et al.* (2013). However, in order to achieve the reliability level required for design and certification purposes, a careful validation in realistic ditching scenarios is essential.

Full-scale testing on aircraft is both impractical and expensive. Scaled model tests are typically used but have the challenge that important physical phenomena are not properly reproduced (Climent *et al.* 2006). The first, very important, limitation concerns the structural behaviour. If strongly nonlinear fluid–structure interaction phenomena are involved, for example, as happens in the presence of permanent deformation, it is impossible to accurately scale the structure and its deformations under the scaled hydrodynamic loading. To overcome this complexity, tests are usually performed on rigid models (Climent *et al.* 2006; Zhang *et al.* 2012). However, there is experimental evidence that the use of rigid models leads to substantial underestimates of the global loading (Iafrati 2015), which is very critical for airframe design and certification.

The limits of scaled model tests are not confined to structural aspects, as important hydrodynamics issues are also involved. In order to properly scale the gravity forces compared with the inertia terms, model tests are performed under the Froude similarity, where the Froude number (Fr) is usually defined as $Fr = U_R/\sqrt{gL_R}$, U_R and L_R being reference values for the velocity and length respectively and g the acceleration of gravity. Therefore, both the velocity and the size are reduced in scaled model tests. Because of the longitudinal and transverse curvatures of the fuselage, suction forces originating in the rear part of the wetted portion of the aircraft have important effects on the aircraft dynamics (McBride & Fisher 1953; Zhang *et al.* 2012). When performing tests at model scale, unless depressurized conditions are used, the ratio between the ambient air pressure p_a and the reference pressure of the flow, $p_R = 0.5\rho U_R^2$, ρ being the water density, is much higher than that at full scale. Thus, the separation/ventilation phenomena that occur in the rear part of the fuselage, and in turn the aircraft dynamics, are not correctly reproduced (Climent *et al.* 2006). Similarly, cavitation phenomena, which may take place depending on the body shape and structural response, cannot be correctly scaled unless the ambient pressure is reduced to achieve the same cavitation number Ca as the full-scale conditions, where $Ca = (p_a - p_v)/(0.5\rho U_R^2)$, p_v being the vapour pressure of the liquid at the local temperature (Brennen 2005).

An experimental investigation of the water entry of a flat rectangular plate with high horizontal velocity is presented in Smiley (1951). Although the work has to be commended for the extraordinary effort and for the quality of the data produced at that time, there were some limits in the experimental set-up which make the measurements not useful for validation purposes. The maximum horizontal velocity was limited to approximately 30 m s^{-1} and diminished substantially during the impact. Furthermore, the sampling rate of the measurements was 1 kHz, too low for accurate description of the pressure time histories (Van Nuffel *et al.* 2013). Finally, the total loads acting on the plate were derived from the acceleration measurements, the latter approach introducing large uncertainties due to the added mass of the water and the inertia and structural response of the facility.

Starting from the above considerations and motivated by the need to obtain a more reliable and complete dataset for the validation of the computational tools and a better understanding of the physical phenomena, an experimental campaign of guided impact tests on rectangular plates was conducted. The plate dimensions were 1000 mm by 500 mm, which is a typical fuselage skin panel size, although the shapes and boundary conditions were different from those of a fuselage panel mounted on a real aircraft structure. Furthermore, at least for the tests presented here, the plates were much thicker than typical thin aeronautical panels. Because of the quite high stiffness, the out-of-plane deformations and the resulting fluid–structure interaction phenomena were negligible, thus making the results essentially independent of the structural behaviour. In this way it is possible to investigate separately the hydrodynamic and fluid–structure interaction aspects. Such a separation of the problems is also useful for the development of software tools as it allows independent validation of the hydrodynamic and structural solvers. Tests were performed at the CNR-INSEAN high-speed ditching facility at horizontal velocities from 30 to 46 m s^{-1}, that is in the lower range of aircraft full-scale ditching velocities.

Test conditions were assigned in terms of three main parameters, which were horizontal velocity, vertical/horizontal velocity ratio (V/U) and pitch angle (α), and were chosen to be representative of aircraft ditching. A detailed description of the facility and the experimental set-up is provided in Iafrati *et al.* (2015), where a preliminary analysis of the data is presented for two specific test conditions with the main purpose of assessing the test repeatability and the uncertainty in the measurements. Hydrodynamic aspects such as the characteristics of the pressure profiles, the time delays of the probes and the curvature of the spray root, the strains and the total loads acting on the plate are discussed, focusing attention on the evaluation of the standard deviation for the different quantities. Important aspects related to the interaction of the flow with the pressure probes are addressed with the aim of identifying spurious phenomena observed in the pressure measurements and distinguishing them from the specific features of the flow. Some aspects concerning the deceleration of the trolley and its effect on the pressure peak intensity are analysed and shown to be rather marginal.

In this paper the physical aspects of the problem are investigated in more depth with the aim of achieving a better understanding of the hydrodynamics and of the role played by the different parameters. Attention is paid to the evaluation of the pressure peak propagation velocity and to its variation during the test as well as to determination of the shapes of the spray root and pressure peak lines. Particular consideration is also given to the identification of the scaling dependences of pressures and loads.

In order to support the analysis and the interpretation of the experimental results, the basic aspects of the water entry of a plate with horizontal velocity are derived from theoretical solutions. Due to the complicated nature of the free-surface evolution in three dimensions, solutions are available within the two-dimensional approximation only. The water entry of a plate with horizontal velocity is studied in Faltinsen & Semenov (2008), where the fully nonlinear self-similar solution is derived for different values of the pitch angle of the plate and of the vertical/horizontal velocity ratio. The latter is, however, much larger than that characterizing the approach trajectories

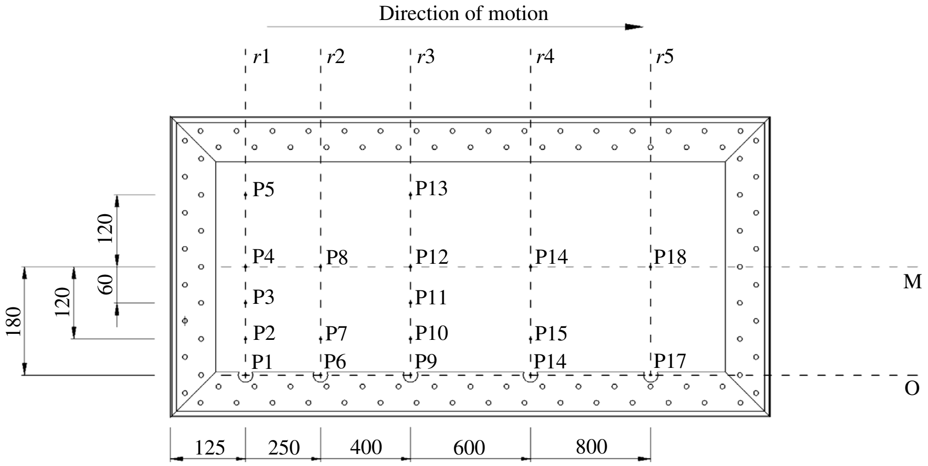

FIGURE 1. The positions of the pressure probes on the plate. Distances are in mm. The probes are distributed along five transverse rows, with indices $r1$–$r5$ moving from the trailing edge to the leading edge, i.e. from left to right. In the following, reference is also made to probes located at the middle of the plate (M), i.e. P4, P8, P12, P16 and P18, and those that are closest to the edge of the plate (O), i.e. P1, P6, P9, P14 and P17.

of aircraft ditching. More appropriate vertical/horizontal velocity ratios are considered in Reinhard, Korobkin & Cooker (2013), where a generalized Wagner approach is exploited and the effects of the elasticity of the plate are also taken into account. Nevertheless, the use of the Wagner approach does not provide accurate information on the pressure distribution. The fully nonlinear solution of the water entry of a flat rigid plate for test conditions similar to those considered here is derived in Iafrati & Calcagni (2013). Before starting the discussion of the experimental measurements, the theoretical model developed in Iafrati & Calcagni (2013) is briefly recalled. The theoretical solution enables the identification of the fundamental features of the flow, as well as the computation of the most significant hydrodynamic parameters which are used to establish comparisons with the experimental data.

2. Experimental set-up

2.1. *Facility and instrumentation*

Experiments were performed at the high-speed impact facility designed and built at CNR-INSEAN within the SMAES project. The facility is composed of a guide, 64 m long, suspended over a water basin, 13.5 m wide, by five bridges. The guide can be rotated, thus allowing V/U ratios in the range 0.03–0.05 to be achieved. The trolley carrying the box structure with the acquisition system and the specimen to be tested is accelerated by a set of elastic cords from rest up to the final speed, and it is left to run freely along the guide during the impact phase. Eventually, the trolley is decelerated by the strong hydrodynamic loads exerted on the front of the box structure when the leading edge of the plate falls below the undisturbed water level.

The plates were instrumented with a total of 18 pressure probes, Kulite XTL 123B, full-scale range 300 Psi absolute, and six biaxial strain gauges. The positions of the pressure probes are shown in figure 1. Accelerations in the three directions were measured through Kistler M101 and M301 resistive accelerometers located at three

U (m s^{-1})	V/U	V (m s^{-1})	α (deg.)	Repeats
40	0.0375	1.50	4	10
34.5	0.0375	1.29	4	1
38.5	0.0375	1.44	4	1
40	0.0375	1.50	6	3
40	0.0375	1.50	10	10
45	0.0333	1.50	4	3
45	0.0333	1.50	6	3
45	0.0333	1.50	10	3
30	0.0500	1.50	10	3

TABLE 1. Test conditions.

different positions around the frame and at the centre of the plate. A total of six acceleration channels were acquired. The loads acting in the direction normal to the plate were measured by four Kistler type 9343 piezoelectric load cells with full-scale range of 70 kN each. Sensor signals were acquired on-board by four Sirius and one Dewe43 Dewesoft modules, controlled by a shock protected computer which was operated as a remote desktop in wireless mode. The sampling rate for the pressure signals was 200 kilosamples per second (kS s^{-1}), whereas all other channels were sampled at 20 kS s^{-1}. The velocity at the initial impact time was measured by a high-speed camera located at the side. The camera was operated at 5000 f.p.s. and the pixel resolution on the measuring plane was 6.2 mm. The impact velocity was computed by using the time taken by the plate to cross a given pixel line, resulting in an uncertainty of ± 0.32 m s^{-1}. The velocity reduction during the test was computed as the integral of the acceleration. A more detailed description of the facility and the set-up is provided in Iafrati *et al.* (2015), where the test repeatability and the inherent uncertainties are assessed as well.

2.2. *Test conditions*

The test conditions were chosen to be representative of aircraft ditching, and variations of single parameters were considered in order to investigate their influence on the results and on the physical phenomena (table 1). The horizontal velocity and the approach angle were decided in order to achieve a vertical velocity of 1.5 m s^{-1}, which is the value to be used in airframe certification as requested by the air-worthiness authorities. Only for the test conditions at 4° and $V/U = 0.0375$ were horizontal velocities below 40 m s^{-1} considered, which led to reduced vertical velocity components. As is discussed in the following, tests that give rise to a reduced loading allow investigation of the influence of the structural deformation of the guide on the measurements.

It is worth observing that in table 1 the nominal horizontal velocity U is provided, whereas the actual horizontal velocity at the impact was within ± 0.5 m s^{-1} of the target value (Iafrati *et al.* 2015). In the analyses presented in the following, the actual velocities derived from the high-speed camera images just before the impact are used in the computation of the scaling factors.

The plate used for the tests was made of an aluminium alloy, AL2024 T351, and it was 15 mm thick, 1000 mm long and 500 mm wide. The plate was clamped to a much thicker aluminium frame over a region 75 mm wide all around, thus leaving an unsupported region in the middle of 850 mm by 350 mm (figure 1). The aluminium frame was connected to the box structure containing the acquisition system and then to the trolley. Although strains were measured, the structural aspects are not discussed here. On the basis of the data, it is estimated that the maximum out-of-plane deformation of the plate was of the order of 0.5 mm, which is rather small to affect the hydrodynamics.

Table 1 shows that several repeats were performed for all cases except for those at reduced vertical velocity. It is worth remarking that tests were performed in a new facility for which there was no preliminary information on test repeatability or on the uncertainties in the measurements. Hence, as discussed in Iafrati *et al.* (2015), it was decided to perform 10 repeats for the tests at $U=40\ \mathrm{m\ s^{-1}}$ at the two limiting pitch angles, i.e. 10° and 4°. At 10° the large number of repeats provides the uncertainty related to the facility itself, which is mainly in the measuring system, initial impact velocity and guide oscillations, whereas the repeats at 4° give an estimate of the increased air-cushion effect. The analysis conducted in Iafrati *et al.* (2015) indicates that for the 10° case the strains and pressures of the different repeats are well overlapped. For the 4° condition, the scatter of the data is still very small for the strains, but it is much larger for the pressure peak values, particularly for the probes located in the first two rows (figure 1). In this case the uncertainty in the data is not associated with the facility but with the air-cushion effects, which are well known to occur when the angle between the plate and the still water level is below 5° (Chuang 1967; Okada & Sumi 2000). Independently of the test conditions, a large scatter of the data is observed for the total loads. In Iafrati *et al.* (2015) it is shown that the scatter of the data for the tests at 4° and 10° is quantitatively similar, but in the former case they appear to be relatively larger because of the lower average value. The independence of the scatter in the amplitude from the specific test conditions indicates that it is mostly associated with oscillations of the guide-rail system.

In the following, depending on the type of analysis, the data are presented either as single repeats or as ensemble averages. In all cases the raw data are provided in order to avoid the introduction of any spurious effect associated with the use of low-pass filters.

3. Data analysis

3.1. *Theoretical solutions of the two-dimensional problem*

In order to understand the fluid dynamics of ditching and to support the discussion of the experimental data, an approximate solution is derived. By following classical approaches to similar water entry problems, the mathematical model is formulated for an inviscid and constant-density fluid, with negligible effects caused by surface tension, gravity and air (Semenov & Iafrati 2006; Faltinsen & Semenov 2008). It is assumed that both the horizontal (U) and vertical (V) velocity components of the plate remain constant during the impact and that the plate is semi-infinite in the longitudinal direction, with the trailing edge of the plate located at $x=Ut$ and $y=-Vt$, where x and y denote the horizontal and vertical axes of an Earth-fixed frame of reference with origin at the initial contact point, $y=0$ being the undisturbed water level. The flow is approximated as two-dimensional, takes place on the (x, y) plane and, on the basis of the above considerations, can be described in terms of the velocity potential $\phi(x, y)$.

As there are no length scales, the problem is self-similar and can be formulated in terms of the new variables

$$\xi=\frac{x}{Ut}, \quad \eta=\frac{y}{Ut}, \quad \varphi=\frac{\phi}{U^2t}. \qquad (3.1a\text{–}c)$$

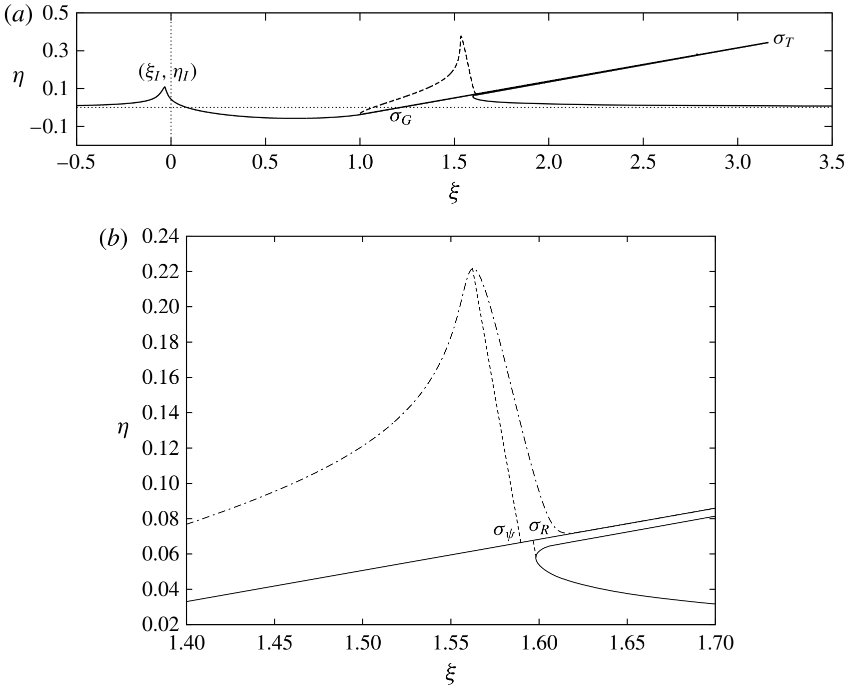

FIGURE 2. (*a*) The free-surface shape obtained by the fully nonlinear potential flow model. The solution refers to the conditions $V/U = 0.0375$, $\alpha = 10^\circ$. The dashed line drawn on the back of the plate represents the pressure distribution (not to scale). (*b*) A close-up view of the spray region. The dashed lines represent the projection on the plate of the pressure peak and spray root and are used to identify the parameters σ_ψ and σ_R.

With the definitions (3.1), the trailing edge of the plate is located at $\xi = 1$ and $\eta = -V/U$.

By following the approach developed in Iafrati & Korobkin (2004, 2008), the initial boundary value problem is transformed into a time-independent boundary value problem, which is solved by the iterative method briefly recalled in appendix A. The free-surface shape for a reference case is shown in figure 2 together with the corresponding non-dimensional pressure distribution

$$\psi = p/(\rho U^2), \tag{3.2}$$

plotted (not to scale) on the back of the plate. The pressure distribution is drawn in figure 3 as a function of the abscissa along the body, σ, the origin of which is at the trailing edge.

Figure 2 shows that, on approaching the plate from the right, the free-surface level rises, takes a sharp curvature at the root, and develops a thin and long spray. The angle formed by the free surface with the plate at the tip of the spray, located at $\sigma = \sigma_T$, is very small but finite. The pressure starts from zero at the trailing edge, increases moving towards the spray root, reaches a peak just behind it, drops abruptly and approaches zero pressure in the spray region. For this reason, in figure 3 the pressure is shown only in a reduced portion of the wetted surface. It is worth noticing that, due to the self-similarity, the farther a point is from the origin, the higher the

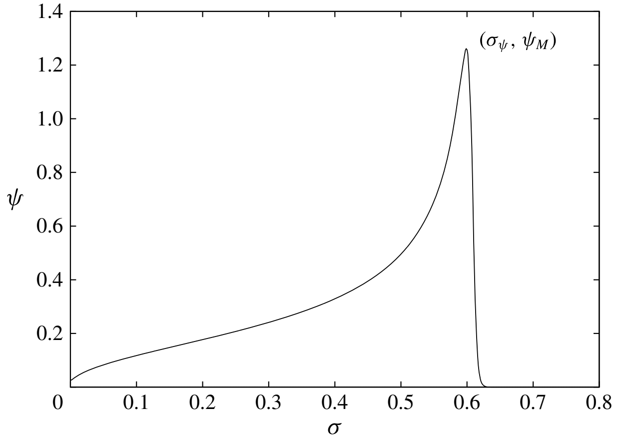

FIGURE 3. The non-dimensional pressure distribution on the plate. It should be noted that the wetted surface is much longer but the pressure is essentially zero in the spray. The solution refers to the case $V/U = 0.0375$, $\alpha = 10^\circ$.

V/U	α	σ_G	σ_R	σ_T	σ_ψ	σ_ψ/σ_G	ψ_M	$\mathscr{F}$	ξ_I	η_I
0.0300	10	0.173	0.535	2.052	0.527	3.046	1.152	0.165	−0.0299	0.101
0.0375	10	0.216	0.608	2.195	0.599	2.773	1.261	0.200	−0.0333	0.111
0.0500	10	0.288	0.726	2.429	0.716	2.486	1.452	0.267	−0.0389	0.128
0.0300	8	0.216	0.586	2.158	0.581	2.690	1.238	0.157	−0.0264	0.107
0.0375	8	0.269	0.673	2.330	0.667	2.479	1.375	0.196	−0.0310	0.106
0.0500	8	0.359	0.812	2.607	0.806	2.245	1.609	0.267	−0.0364	0.123
0.0300	6	0.287	0.773	2.536	0.770	2.683	1.556	0.182	−0.0279	0.095
0.0375	6	0.359	0.894	2.778	0.891	2.482	1.774	0.233	−0.0317	0.107
0.0500	6	0.478	1.079	3.145	1.075	2.249	2.135	0.329	−0.0369	0.136
0.0300	4	0.430	1.001	2.998	1.000	2.326	1.987	0.194	−0.0252	0.105
0.0375	4	0.538	1.189	3.373	1.188	2.208	2.384	0.265	−0.0302	0.115
0.0500	4	0.717	1.416	3.824	1.414	1.980	2.883	0.396	−0.0363	0.128

TABLE 2. Parameters identifying the key aspects of the fully nonlinear solution for the free-surface shape, pressure distribution and total load.

speed is. As both the pressure peak, spray root and spray tip are located at $\xi > 1$, they are all faster than the plate. In the rear part, the free surface leaves the plate tangentially, rises up to a maximum which is reached just behind the initial contact point $\xi = 0$ and gradually approaches the undisturbed water level $\eta = 0$ as $\xi \to -\infty$.

In order to compare solutions for different impact conditions, some basic parameters are identified in figure 2 and figure 3 and reported in table 2. Some of the parameters denote the relevant points of the free-surface shape in terms of the abscissa along the plate, σ. The most relevant for the analysis to be carried out in the following are the geometric intersection point between the plate and the still water level, located at $\sigma = \sigma_G$, where $\sigma_G = V/(U \sin\alpha)$, the spray root, located at $\sigma = \sigma_R$, and the spray tip, located at $\sigma = \sigma_T$. Other parameters are the non-dimensional coordinates (ξ_I, η_I) of the inversion point, the pressure peak, which is located at $\sigma = \sigma_\psi$ where it takes a non-dimensional value $\psi = \psi_M$, and, finally, the non-dimensional value of the normal

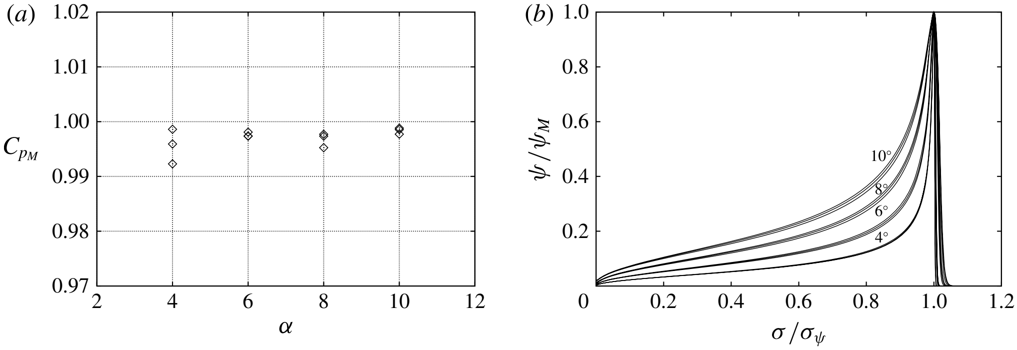

FIGURE 4. (*a*) The peak values of the pressure coefficient given by (3.4) for the different conditions. (*b*) The pressure distributions obtained for different pitch angles are drawn by using the peak intensity ψ_M and its abscissa σ_ψ to scale the vertical and horizontal axes respectively. The data indicate that the scaled pressure distribution has a larger area, i.e. a higher load, on increasing the pitch angle, whereas the effect of the V/U ratio is very small.

load acting on the plate per unit of transverse length, denoted by $\mathscr{F}$. The latter is related to the dimensional term, $F(t)$, by the following relation:

$$\mathscr{F} = \frac{F(t)}{\rho U^3 bt}, \tag{3.3}$$

where b is the breadth of the plate, which is $b=1$ in the two-dimensional assumption.

The data in table 2 show that ψ_M varies substantially with the test conditions. As ψ_M is derived from (3.2), such large variation indicates that U^2 is not the proper scaling factor for the pressure peak. By recalling the basic features of water entry flows (Cointe & Armand 1987; Howison, Ockendon & Wilson 1991), the pressure peak should correlate to the square of the velocity in the x-direction of the spray root, $U(1+\sigma_R\cos\alpha)$, or to the square of the propagation velocity of the pressure peak which is approximately the same, $U(1+\sigma_\psi\cos\alpha)$. The above hypothesis is indeed confirmed by the data provided in figure 4(*a*), which show that the peak pressure coefficient

$$C_{pM} = \frac{\psi_M}{\frac{1}{2}(1+\sigma_\psi\cos\alpha)^2} \tag{3.4}$$

is nearly one for all impact conditions.

Although the square of the horizontal velocity of the spray root is representative of the peak value, the pressure distribution along the plate also depends on the normal velocity of the relative flow, U_n, which varies with both the V/U ratio and the pitch angle as

$$U_n/U = \sqrt{1+(V/U)^2}\ \sin(\alpha+\beta), \tag{3.5}$$

where $\beta = \arctan V/U$ is the inclination angle of the guide. Such dependence can be easily recognized by the scaled pressure distributions reported in figure 4(*b*), which display a significant variation with the pitch angle, whereas the V/U velocity ratio plays a less relevant role.

The solution and results derived above are used in the following as a basis for the discussion of the experimental data. However, several important assumptions are made in the derivation of the model which have to be accounted for when establishing comparisons. According to Korobkin & Pukhnachov (1988), the effects of liquid compressibility are negligible in the water entry of pointed bodies, which is the case considered here. Viscous effects might have an effect in the spray region where strong velocity gradients occur, but considering the quite high Reynolds number of the flow, $Re = U_R L_R/\nu \simeq 4 \times 10^7$, ν being the kinematic viscosity of water, the impact loads are essentially independent of them (Moghisi & Squire 1981). The dynamics of the spray as well as its stability are also influenced by surface tension effects, as is briefly discussed at the beginning of the next section, but a detailed description of the spray region is out of the scope of the present work. For the problem under consideration, gravity is rather small compared to the inertia, $Fr = U_R/\sqrt{gL_R} \simeq 13$, and there is experimental evidence that in such conditions there are no significant effects on the loads and on the spray root dynamics (Zhao, Faltinsen & Aarsnes 1996), although the dynamics of the spray may be affected to some extent. Finally, comparisons between experimental data and numerical results for the water entry of finite wedges (Zhao *et al.* 1996; Zhao, Faltinsen & Haslum 1997; Iafrati & Battistin 2003) indicate that the assumption of a semi-infinite plate, which is essential for the self-similarity of the solution, is acceptable at least up to the time when the spray root reaches the leading edge of the plate.

Because of the peculiarities of the facility and of the experimental set-up and conditions, other assumptions deserve more careful consideration. In particular, it is important to evaluate the role played by the air, by the variation of the test velocity due to both deceleration of the trolley and oscillation of the guide as well as by the third dimension. The latter especially is expected to have a significant influence as the transverse breadth of the plate is only half the plate length and thus the possibility for fluid to escape from the side may affect the spray root propagation velocity, the pressure distribution and, consequently, the loads. The effect of the three-dimensionality on the loads is theoretically addressed in Korobkin & Scolan (2006), whereas the strong changes in the spray root propagation velocity, pressure distribution and loads when passing from a two-dimensional wedge or cylinder to the corresponding axisymmetric shape, cone or sphere, are clearly highlighted in Battistin & Iafrati (2003). The above aspects are discussed in the following with the aim of explaining the deviation of the experimental results from the theoretical model.

3.2. *Experimental results for the pressure peak propagation velocity*

On the basis of what has been discussed so far, as soon as the plate touches the water surface, a thin spray develops and propagates along the plate, becoming longer and longer as the plate penetrates. The spray formation and propagation can be seen from the sequences of underwater images provided in figures 5(*b*,*d*,*f*,*h*,*j*) and 6(*b*,*d*,*f*). In order to help in the interpretation of the images, dashed lines are drawn along the sides of the plate and a solid line is drawn at the spray root. The plate is moving from left to right and the spray develops on the right of the spray root. The underwater images show that the spray root is not exactly straight but develops a curved shape as a consequence of outflow at the sides, as is discussed below. A preliminary discussion on the spray root shape and on the differences observed for the 4° and 10° pitch angles is provided in Iafrati *et al.* (2015), whereas a much deeper and more quantitative analysis of the spray root is presented in the next section.

Just to give an estimate of the tip velocity, from the underwater images in figure 5(*b*,*d*,*f*,*h*) it is seen that, for the selected test conditions, the spray tip reaches

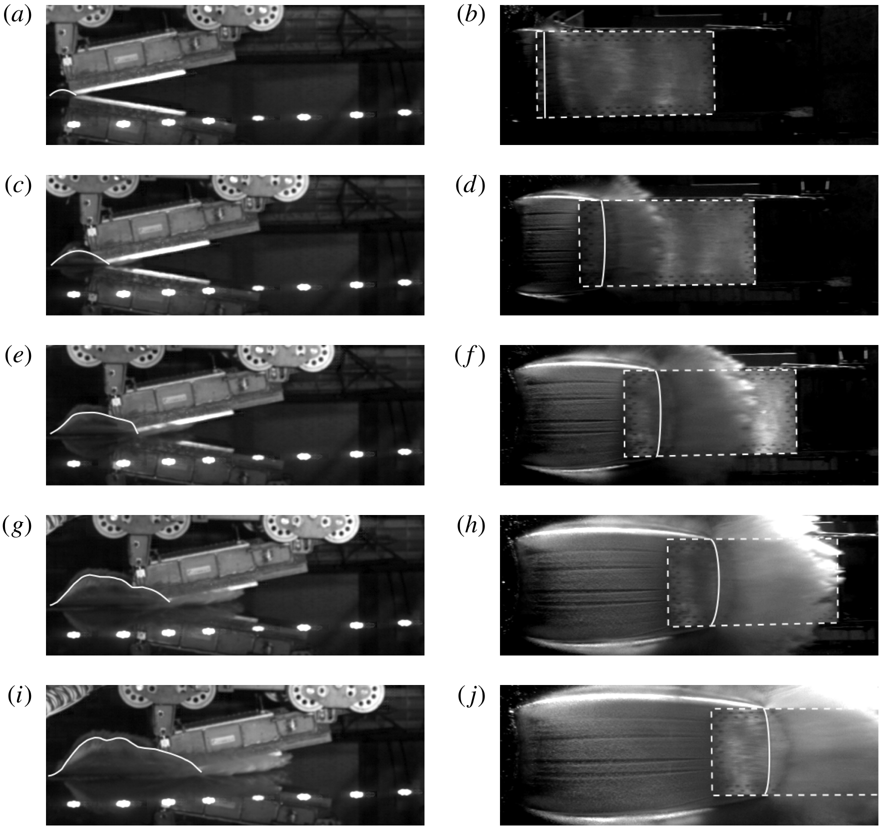

FIGURE 5. Impact sequence for test conditions of 45 m s^{-1}, 10°. Images from the side and underwater cameras are shown in (*a*,*c*,*e*,*g*,*i*) and (*b*,*d*,*f*,*h*,*j*) respectively. The plate is moving from left to right and the time interval between two successive images in the sequence is 0.005 s. In (*a*,*c*,*e*,*g*,*i*), the white solid lines are used to highlight the tip of the splash released on the side as a result of three-dimensional effects. In (*b*,*d*,*f*,*h*,*j*), the white solid lines are used to locate the spray root, whereas the dashed lines are drawn about the contour of the plate.

the leading edge of the plate approximately 0.015 s after the first contact. Since the plate is 1 m long, the propagation velocity of the spray tip along the plate is of the order of 66 m s^{-1}, which corresponds to an absolute horizontal velocity of the order of 110 m s^{-1}. Because of such high speed and the interaction with the air and with the plate surface, the thinnest part of the spray is fragmented into tiny droplets, the size of which is governed by surface tension (Iafrati *et al.* 2015).

The images from the camera at the side provided in figure 5(*a*,*c*,*e*,*g*,*i*) show the development of two water splashes at the sides of the plate. A white solid line is drawn to highlight the tip of the splash located on the side closest to the camera and to distinguish it from the one located on the opposite side. Such splashes are a consequence of the flow outgoing from the side of the plate due to the finite breadth, which in fact is a three-dimensional effect. The splashes generated for different pitch angles are shown in figure 6(*a*,*c*,*e*). The three images, which are taken at the same penetration depth, indicate that the splash is stronger for larger pitch angle. The more intense outflow generated for larger pitch angles is associated with the higher value of

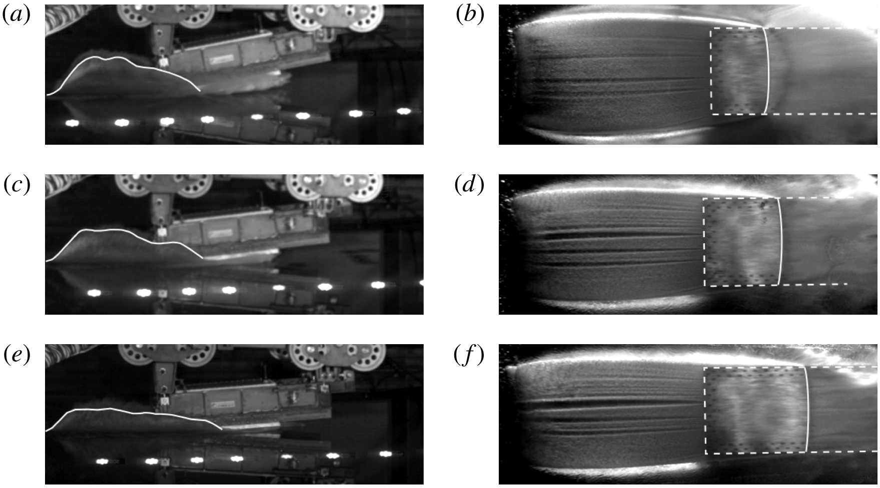

FIGURE 6. Images from the side and underwater cameras taken at the same penetration depth for different pitch angles: (*a*,*b*), (*c*,*d*) and (*e*,*f*) show the 10°, 6° and 4° conditions. The images refer to 45 m s^{-1} horizontal velocity. The white lines have the same meaning as in figure 5.

the normal velocity component (3.5) and, consequently, with the higher mean pressure value on the plate (figure 4*b*). The above result supports the expectation that three-dimensional effects are more important for larger pitch angles.

In the previous section it was explained that the pressure peak is strongly correlated with the spray root propagation velocity. Moreover, it was seen that from the theoretical solution, the propagation velocity of the spray root is very close to that of the pressure peak, and indeed the latter was used for the computation of the corresponding pressure coefficient from (3.4). Even though the result is well known and accepted in the field of water entry (Cointe & Armand 1987; Howison *et al.* 1991), it is worth verifying whether a similar relation holds for the present experimental data.

Unfortunately, as shown in figures 5 and 6, due to the too poor spatial and temporal resolution, the underwater images do not allow reliable estimates to be derived for the spray root propagation velocity and the only possibility is to exploit the pressure measurements and use the pressure peak propagation velocity for the scaling. To this purpose, the time interval taken by the pressure peak to reach different probes located at the same transverse position is computed first. The probe P4, located in the middle of the plate on the first sensor row $r1$ (figure 1) is used to define the reference for the time. The time delay τ_j taken by the pressure peak to reach the jth probe is computed as the time shift leading to the maximum correlation between the pressure history recorded at P4 and that at Pj (Iafrati *et al.* 2015).

The time delays for the test conditions at 40 and 45 m s^{-1} are shown in figure 7. The vertical coordinate s_P denotes the longitudinal position of the pressure peak that coincides with that of the jth pressure probe when $t=\tau_j$. It should be noted that hereafter s indicates the abscissa along the plate, with origin at the trailing edge. For all impact conditions the data follow nearly linear trends, with the propagation velocity of the pressure peak along the plate being somewhat higher than that of the geometric intersection, $U\sigma_G$ or $V/\sin(\alpha)$.

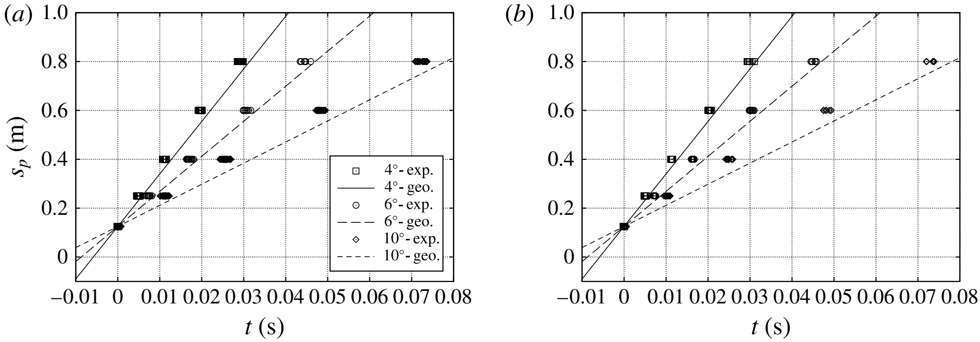

FIGURE 7. Time delays of the probes for the different test conditions. The data in (*a*) and (*b*) refer to the tests at 40 m s^{-1} and 45 m s^{-1} respectively. The vertical coordinate s_P denotes the distance of the probe from the trailing edge measured along the plate. The straight lines represent the position along the plate of the geometric intersection point computed as $Vt/\sin\alpha$, where V is the nominal value of the vertical velocity.

Starting from the longitudinal positions of the probes and the time delays τ_j, the propagation velocity of the pressure peak along the plate is computed by a second-order finite difference scheme, and its projection on the x-axis is denoted by u_P. The propagation velocity can be computed by using the data of probes located at the same transverse position. Hence, this is done for probes located along the midline of the plate, i.e. P4, P8, P12, P16, P18, which are referred to as M, and for those located at the side, i.e. P1, P6, P9, P14, P17, which are referred to as O (figure 1). The propagation velocities computed for the tests at 40 and 45 m s^{-1} and for the different pitch angles are provided in figure 8. In order to facilitate the comparison between the different test conditions, the horizontal component of the pressure peak propagation velocity is scaled by the horizontal velocity of the geometric intersection point, $u_G = U\sigma_G \cos\alpha = V/\tan(\alpha)$. The data indicate that the ratio u_P/u_G diminishes as time elapses and the plate penetrates into the water, with maximum values in the range 1.3–1.6 and minimum values in the range 0.90–1.05.

The variation of the propagation velocity with time already indicates that the behaviour is not self-similar. In order to establish more quantitative comparisons with the theoretical solutions, it is worth recalling that, in terms of the notation introduced in the previous section, the horizontal component of the pressure peak propagation velocity along the plate is $U\sigma_\psi \cos\alpha$, U being the nominal test speed, and hence u_P/u_G should be compared with σ_ψ/σ_G. The data provided in table 2 show that this ratio is between 2 and 3, with lower values obtained for smaller pitch angles. In all cases the theoretical values are much higher than the experimental values.

Similar conclusions may be derived by the analysis of the experimental data reported in Smiley (1951). At least for the test condition referred to as Run 8 in the report, the times of the pressure peak occurrence at the different probes, and thus the corresponding propagation velocities, can be retrieved from the curves provided in figure 2, on p. 29 of the report. The test conditions are $U = 19.05$ m s^{-1}, $V = 1.585$ m s^{-1}, 12° pitch angle. It should be noted that in Smiley (1951) the aspect ratio of the plate is 5 instead of 2 for the present test conditions. The extracted data, which are reported in figure 9, exhibit the same behaviour as the present experiments even though the u_P/u_G velocity ratio displays a much stronger reduction, with the

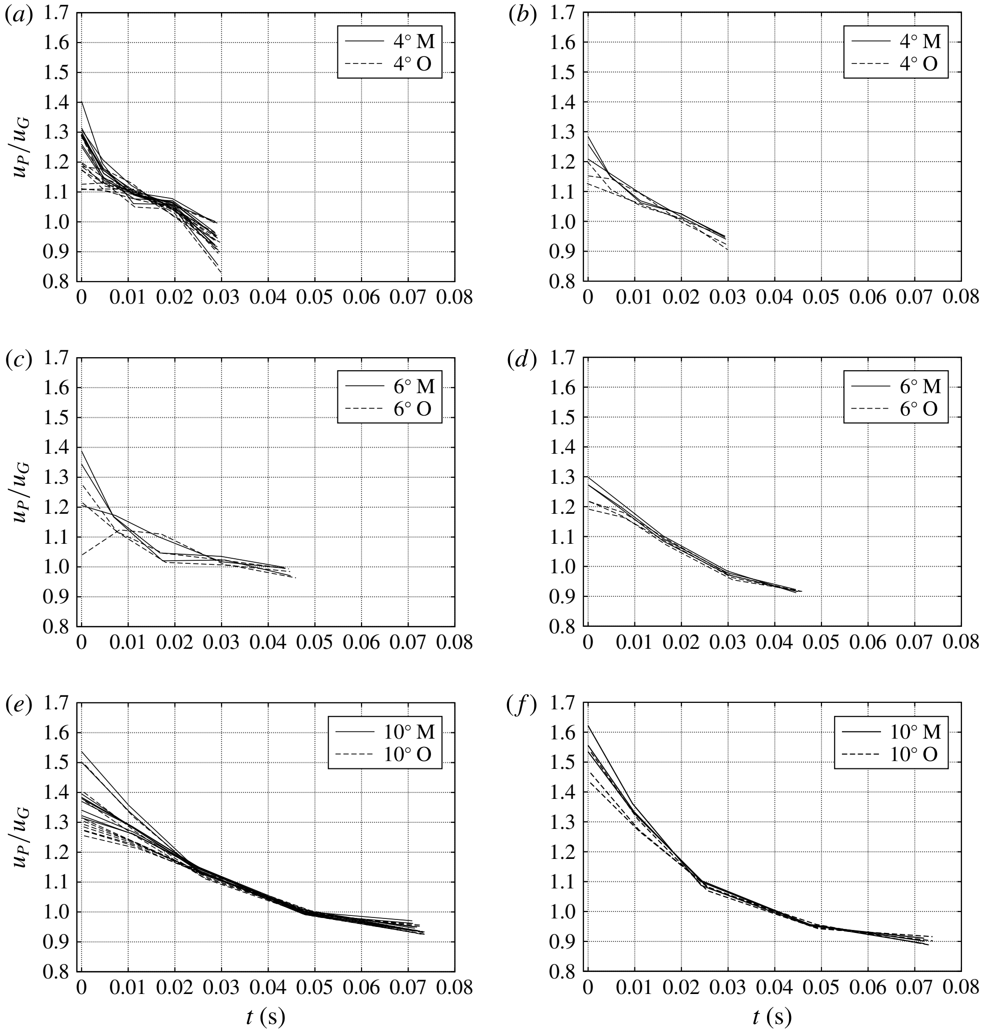

FIGURE 8. The propagation velocity of the spray root, u_P, scaled by the propagation velocity of the geometric intersection point, u_G. The results in (*a*,*c*,*e*) and (*b*,*d*,*f*) refer to tests at 40 m s^{-1} and 45 m s^{-1} respectively. The data for all test repeats are drawn in order to provide an estimate of the related uncertainty.

propagation velocity dropping below one third of the propagation velocity of the geometric intersection point.

As anticipated at the end of the previous section, in order to better understand the reasons for the large reduction in the propagation velocity of the pressure peak with respect to that of the geometric intersection point, the role played by some of the assumptions made in the derivation of the theoretical model has to be investigated. In particular, bearing in mind the basic features of the solution discussed in the previous section, it is difficult to justify a propagation velocity of the pressure peak below that of the geometric intersection point, i.e. $u_P/u_G < 1$, as occurs at the end of the curves in figure 8.

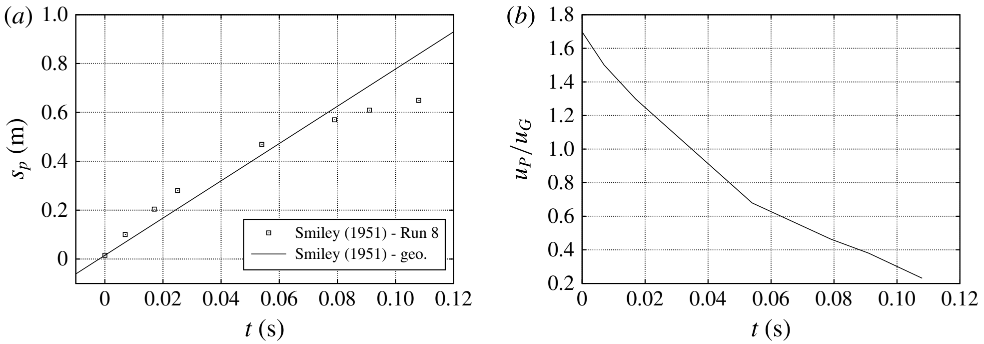

FIGURE 9. (*a*) The time delays of the probes as derived from the data of figure 2 in Smiley (1951). The corresponding values of the propagation velocity scaled by the velocity of the geometric intersection point are given in (*b*).

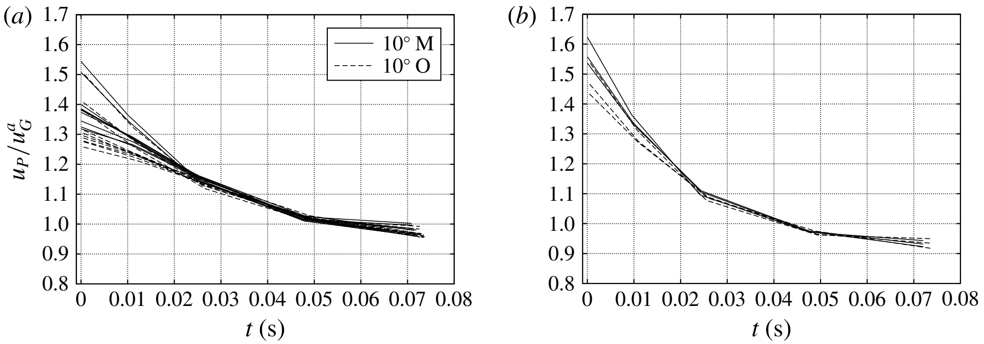

FIGURE 10. The time histories of the u_P/u_G ratio for the tests at 10° at 40 m s^{-1} (*a*) and 45 m s^{-1} (*b*). The deceleration of the trolley is accounted for in u_G^a.

A first point deserving consideration is the value of u_G adopted for the scaling. The curves in figure 8 are drawn by using the nominal value of u_G computed as $V/\tan\alpha$, and thus the deceleration of the trolley during the tests is not taken into account. For instance, the data of Run 8 provided in table II of Smiley (1951) indicate that during the impact the vertical velocity undergoes a reduction by a factor of 1/3.5, and thus the nominal value of u_G greatly overestimates the propagation velocity of the geometric intersection point, which explains most of the reduction observed in figure 9(*b*).

In order to derive an improved estimate of the propagation velocity of the geometric intersection point, the velocity reduction during the impact phase is computed as the time integral of the acceleration, and the actual horizontal velocity of the trolley, $U_a(t)$, is obtained by subtracting the velocity reduction from the initial impact velocity. For the present experimental campaign, thanks to the quite high mass of the trolley, the velocity reduction is very small, being of the order of 0.5 m s^{-1} in the 4° case and 2 m s^{-1} in the 10° case (Iafrati *et al.* 2015). By using the instantaneous entry velocity, the actual propagation velocity of the geometric intersection point is computed as $u_G^a = U_a(t)\sigma_G \cos(\alpha)$. The data for u_P/u_G^a are provided in figure 10 for the tests at 10°, which are characterized by the largest velocity reduction. Apart from a small increase compared with u_P/u_G that can be observed at the end of the curves, $u_P/u_G^a < 1$ still holds. Hence, the deceleration of the trolley is not sufficient to explain

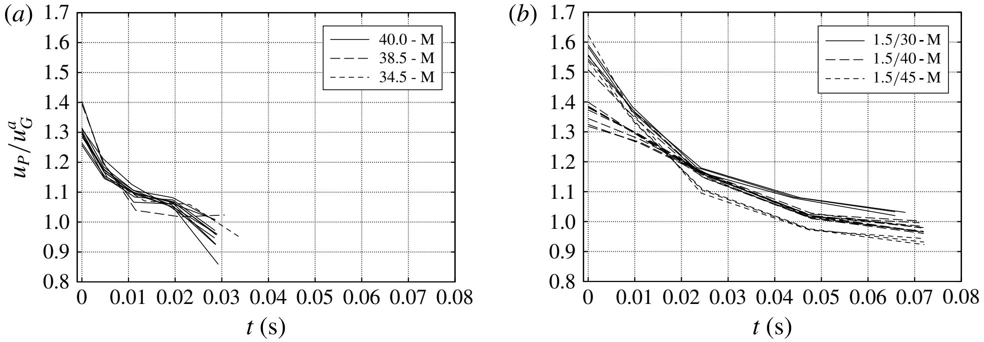

FIGURE 11. Effect of the test speed and of the guide inclination on the propagation speed. In both cases the data at the end of the tests indicate that higher values of u_P/u_G^a are obtained for lower horizontal speed.

the propagation velocity of the pressure peak being below that of the geometric intersection.

In addition to the effect of the deceleration on the horizontal velocity, the vertical velocity of the plate may also vary as a consequence of the structural deformation of the guide when exposed to the high loads generated during the impact. Such variations have direct consequences on the propagation velocity of both the pressure peak and the geometric intersection point.

Quantitative estimates of the vertical displacement and velocity measured at one point of the guide are provided in Iafrati *et al.* (2015) for one of the tests performed at 40 m s^{-1}, 10°. In the early phase, the vertical velocity displays oscillations about a non-zero value with a period of approximately 0.0125 s and maximum upwards values of the order of 0.3 m s^{-1}. In the next stage, the period rises to approximately 0.025 s and the amplitude of the oscillations grows: the vertical velocity of the guide changes from upwards to downwards and takes peak values of approximately 0.5 m s^{-1}. In the very late stage of the entry process, just before the spray root leaves the plate, the velocity reaches a peak value of approximately 0.7 m s^{-1} upwards. Of course the occurrence of upwards velocity leads to reductions in the pressure peak propagation velocity, in the pressure values and in the total loading. In particular, the upward velocity of 0.7 m s^{-1}, being approximately half of the nominal value, is expected to have relevant effects. However, as explained, such a high value occurs in a very late stage of the entry process lasting approximately 0.01 s, which is well beyond the stage considered in the above discussion. Furthermore, for the tests at 10° the impact phase lasts approximately 0.1 s, and considering the period of oscillations, it appears to be more reasonable to filter them out by computing an average vertical velocity based on the displacement. By using this approach it is estimated that during the impact phase the guide has an average upwards velocity of approximately 0.076 m s^{-1}, which is approximately 5 % of the nominal value. As the structural deformation of the guide is not accounted for in the evaluation of u_G^a, the reduction in the average vertical velocity and the corresponding reduction in the propagation velocity of the geometric intersection point explain the occurrence of $u_P/u_G^a < 1$ in some conditions.

Detailed data on the guide bending are not available for all test conditions, but it is reasonable to expect that the structural deformations are smaller for lower hydrodynamic loads. In order to further investigate this aspect, in figure 11 two comparisons are established. In figure 11(*a*) the data for three tests performed at the same V/U and pitch angle but at different horizontal speeds are provided. As is discussed in the following, the loads scale as the square of the normal velocity component, and thus the loads generated during the tests at 34.5 m s^{-1} are approximately 30 % smaller than those at 40 m s^{-1} (figure 24). Despite such significant reduction in the loading, no substantial differences are found in terms of u_P/u_G^a (figure 11*a*). Another comparison is presented in figure 11(*b*). Again, the horizontal speed is varied, but in this case both the vertical velocity and the pitch angle are kept constant. From the data provided in figure 25 it is seen that in the tests at 30 m s^{-1} the normal loading on the plate is approximately 45 % of that measured at 40 m s^{-1} and even smaller compared with the 45 m s^{-1} condition. Nonetheless, again, in spite of the large reduction in the loading, a limited increase of approximately 10 % is observed at the end of the curves. Such an increase is, however, found to always have $u_P/u_G^a > 1$ for the 30 m s^{-1} condition.

From the above considerations, it is follows that, even accounting for the reduction of the deceleration of the trolley and for the upwards velocity induced by the structural deformation of the guide, the propagation velocity of the pressure peak remains much lower than that predicted by the two-dimensional approximation, and in any case it diminishes substantially as the plate penetrates, gradually approaching that of the geometric intersection point.

It is speculated here that both the lower value of the pressure peak propagation velocity and its reduction during the impact are consequences of the three-dimensionality of the problem. Such a statement could only be confirmed through additional tests performed on plates of different breadth or by numerical simulations of the full three-dimensional flow. However, important arguments to support the above conjecture are provided in Battistin & Iafrati (2003), where the free-surface profiles generated during the water entry of a wedge and a cylinder are compared with the profiles obtained for the corresponding cone and sphere. Whereas the propagation velocity of the geometric intersection point is the same, the results clearly show that in the axisymmetric cases, when the fluid can move in all directions, the propagation velocity of the pressure peak, or of the spray root, is much smaller than that in the two-dimensional configuration. For the rectangular plate considered here, the ratio between the longitudinal and transverse dimensions of the wetted area grows in time, and the two quantities become comparable in approximately the middle of the impact phase. Hence, in the first half of the entry process the free-surface flow undergoes a transition from quasi-two-dimensional to a fully three-dimensional one, and that is in fact the phase during which the sharp reduction in the u_P/u_G ratio is observed.

3.3. *Pressure peak line and spray root shapes*

The underwater images in figures 5 and 6 show that the spray root is characterized by a backward curvature, with the foremost point reached at the middle of the plate. Here and in the following, the curvature is intended in an average sense to indicate the amount of bending of the spray root line. As already anticipated in the previous section, the curvature of the spray root is a consequence of the three-dimensionality and of the possibility for the fluid to exit from the sides. Therefore, a quantitative estimate of the spray root shape provides important insights into the hydrodynamics and into the effects of the third dimension and the pitch angle. Being very sensitive to the flow features, the spray root shape is also very useful for the validation of computational approaches.

As mentioned above, the quality of the underwater images in terms of pixel resolution, sharpness and contrast is too poor and does not allow the spray root shape to be retrieved accurately. In § 3.1 it has been explained that the spray root is just ahead of the pressure peak location (see figure 2(*b*) and data in table 2) and, thus, instead of the spray root shape, the pressure peak line is derived here starting from the pressure measurements, as is explained in the following.

The high sampling rate of the measurements provides very accurate information on the time at which the pressure peak crosses each probe. Therefore, the shape of the pressure peak line can be evaluated from the times at which the pressure peak reaches the probes located at the same longitudinal position, i.e. located along the same sensor row. If all of the probes located along the same sensor row are reached by the pressure peak at the same time, the pressure peak line is just straight. Alternatively, the shape of the pressure peak line is estimated by multiplying the time differences between the probes by the pressure peak propagation velocity computed in the previous section. Of course there is a test-to-test dispersion of the data in terms of either the time differences or the propagation velocity. Some data concerning the dispersion of the time delays as well as some considerations about the symmetry of the data are presented in Iafrati *et al.* (2015), whereas the scatter in the pressure peak propagation velocity can be estimated from the data shown in the previous section. In the following the results are presented in terms of the ensemble average over all of the repeats performed at the same test conditions.

The time delays with respect to the probe lying in the same row at the middle of the plate are shown in figure 12 for the different test conditions. The data are presented for the right side of the plate, i.e. $z \leqslant 0$, where most of the probes are located (figure 1). The data in figure 12(*a*,*b*) show that for the 4° condition, the distribution of the time delays in the first sensor row $r1$ is quite different from the other cases and, furthermore, negative time delays are also found. Negative time delays mean that the pressure peak reaches the probes located at the side earlier than that at the middle. This phenomenon, already discussed in Iafrati *et al.* (2015), is associated with the air-cushion effect which is relevant for the 4° case, whereas it is much less important for larger pitch angles due to the increased possibility for air to escape from the side (Chuang 1967; Okada & Sumi 2000).

A quantitative estimate of the free-surface deformation caused by the air-cushion effect can be derived by computing the stagnation pressure of the airflow with respect to the plate. For the 4° case at 45 m s^{-1}, the normal velocity component of the relative airflow is $V \cos \alpha + U \sin \alpha = 4.64$ m s^{-1}, and therefore, for an air density of 1.25 kg m^{-3}, the stagnation pressure is $P_s = 13.46$ Pa, which corresponds to a water column of 1.37 mm. For a vertical entry velocity of 1.5 m s^{-1}, this implies that the lowest part of the free surface is touched by the plate approximately 915 µs after the plate edges. Such an estimate is consistent with what was found from the analysis of the underwater movie, not presented here, which shows that it takes approximately 3 frames, or 1000 µs, for the trailing edge to be fully wetted. As soon as the spray root starts to move along the plate, the initial effects of the air cushion are compensated by the three-dimensionality of the flow and, as shown in figure 12(*a*,*b*), already at the first sensor row, the time delays are an order of magnitude smaller.

Moving forward along the plate, as already observed in Iafrati *et al.* (2015) on the basis of the data for the two test conditions at 40 m s^{-1}, 4° and 10° pitch angles, there is a growth in the time delays of the probes located away from the midline. The time delays measured in the tests at 40 m s^{-1} are generally larger than those measured in the tests at 45 m s^{-1}, which can be explained by the higher propagation velocity of the pressure peak for higher horizontal velocities.

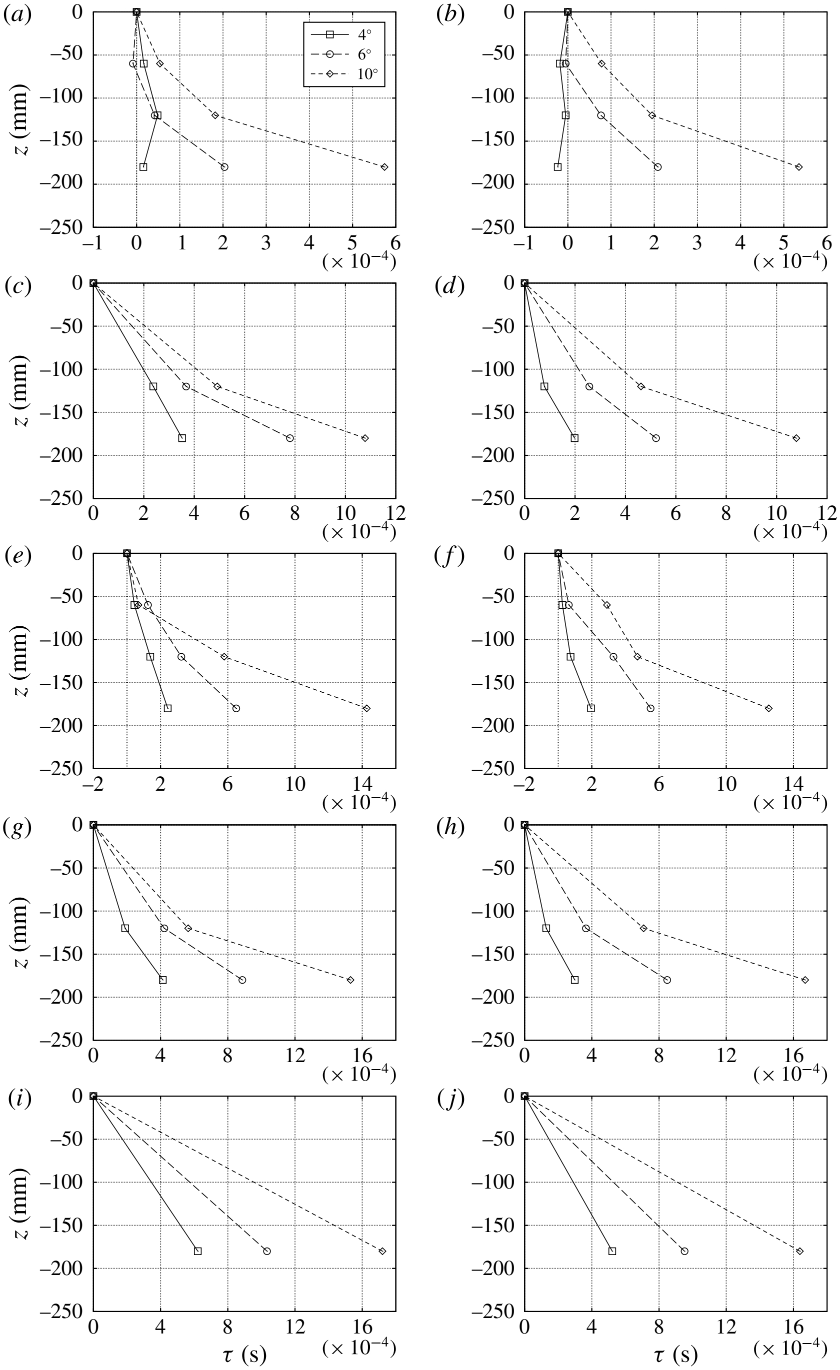

FIGURE 12. Ensemble averages of the time delays of the probes located in the five rows of pressure probes computed with respect to the probe located in the same row at the middle of the plate ($z = 0$). The longitudinal coordinate of the row grows from top to bottom (figure 1). The data in (a,c,e,g,i) and (b,d,f,h,j) refer to tests at 40 m s^{-1} and 45 m s^{-1} respectively. It should be noted that lines are only drawn with the purpose of connecting points belonging to the same test condition.

As explained above, the shape of the pressure peak line is obtained by multiplying the time delays provided in figure 12 by the pressure peak propagation velocity as computed in the previous section. Since the propagation velocity of the pressure peak is obtained by numerical differentiation, it may introduce additional errors to the results. Moreover, the available data do not allow any estimate concerning the variation of the propagation velocity in the transverse direction to be extracted, and therefore the pressure peak lines are computed by assuming the propagation velocity to be uniform in the transverse direction and equal to the value it takes in the middle of the plate for each sensor row.

The data for the pressure peak line are presented in terms of the ensemble average of the shapes computed for the different repeats of the same test conditions (figure 13). The results show that the curvature of the line grows moving forward along the plate. However, there are also cases in which the curvature at row *r*2 seems to be larger than that at row *r*3 (e.g. figure 13*a*–*c*). On the other hand, the data in figure 12(*c*,*e*,*f*) indicate that the time delays are still growing and, thus, the larger curvature observed at row *r*2 compared with that at row *r*3 can be related either to the errors in the computation of the propagation velocity or to the oscillations in the vertical velocity induced by the structural deformations of the guide.

Another conclusion that can be drawn from the data is that for the 10° case the pressure peak line quickly develops its final shape and the curvature at row *r*2 is approximately the same as that at row *r*5. On the contrary, for smaller pitch angles the growth of the curvature is slower and more regular. The interesting aspect is that at row *r*5 the Δs between P18 and P17 is essentially the same for all test conditions. With regard to the latter aspect, from the data in figure 12 it is seen that the time delays at row *r*5 are generally larger for larger pitch angles. This result means that the difference in time is compensated by the difference in the pressure peak propagation velocity, which is lower for larger pitch angles.

The faster growth of the curvature at larger pitch angles and the similar shapes of the pressure peak lines occurring at row *r*5 are also observed for the spray root lines displayed in the underwater pictures (figure 14). Figure 14(*a*) and (*b*) for the 10° and 4° cases respectively refer to a time T1 at which the spray roots are approximately 0.40 m ahead of the trailing edge of the plate, which means at row *r*3. By comparing them, it can be noticed that for the 10° case the spray root exhibits a noticeable curvature already, whereas for the 4° case the curvature is less pronounced. A similar comparison is established in figure 14(*c*,*d*), for a later stage. The two images correspond to a time T2 at which the spray is approximately 0.65 and 0.80 m ahead of the trailing edge for 10° and 4° respectively. The 0.80 m distance from the trailing edge means that the spray is at sensor row *r*5. Due to the different inclination of the plate, for the 10° condition the spray reaches sensor row *r*5 outside the field of view of the underwater camera, and thus a shorter distance is considered. Even though the light level is quite low, it is observed that in the 10° case the shapes of the spray root at the two times are comparable, whereas in the 4° case there is a noticeable increase in the curvature. Moreover, the curvature in figure 14(*d*) looks quantitatively similar to that in figure 14(*a*), in agreement with what has been found in terms of the pressure peak line.

All of the above considerations are supported by the data shown in figure 15, where the spray root lines drawn on the underwater images of figure 14 are digitalized and plotted together with the data available for the pressure peak lines. The spray root is provided in terms of both the digitalized points and their Bezier interpolation. From the comparison of the spray root lines obtained at the two times for 10° it is seen

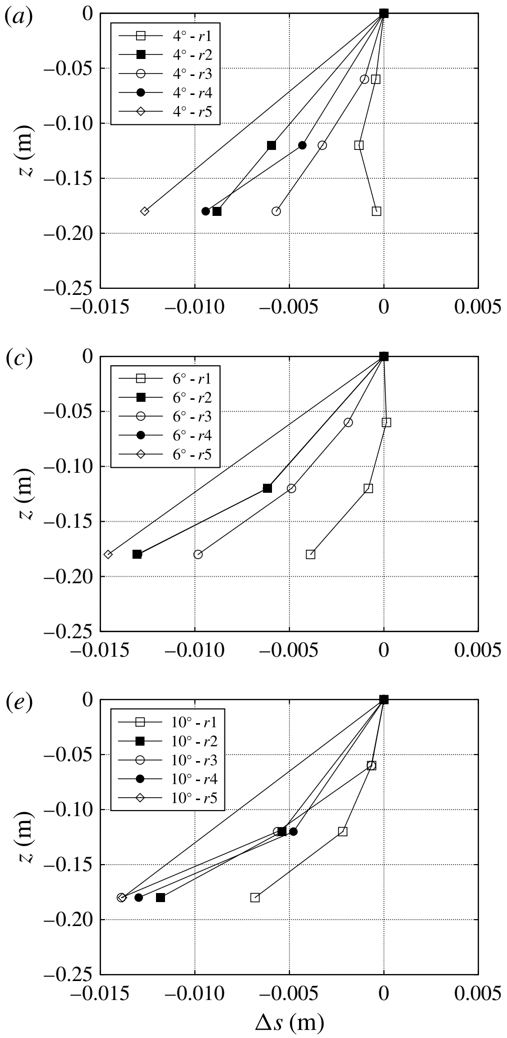

FIGURE 13. The shapes of the pressure peak lines computed as the product of the time delays of the different probes by their propagation velocities. The results in (*a*,*c*,*e*) and (*b*,*d*,*f*) refer to the tests performed at 40 m s^{-1} and 45 m s^{-1} respectively. As in figure 12, data are obtained from the ensemble average over the different repeats and are computed for the right side of the plate, $z \leqslant 0$, where most of the probes are located (figure 1). In the keys, *r*1–*r*5 indicate the five sensor rows and the lines are drawn with the only purpose of connecting points belonging to the same row.

that the shapes are essentially unchanged, confirming that for the large pitch angle the spray root develops its final shape rapidly. On the contrary, for the 4° case, the curves display a more regular growth, in agreement with what has been observed on the basis of the pressure peak lines. Bearing in mind the limits in the pixel resolution, which can be argued by the distributions of the symbols, the data in figure 15 also support the fact that, in a later stage, the spray root approaches the same shape independently of the pitch angle. Finally, a quite satisfactory quantitative agreement is found between the spray root and the pressure peak lines.

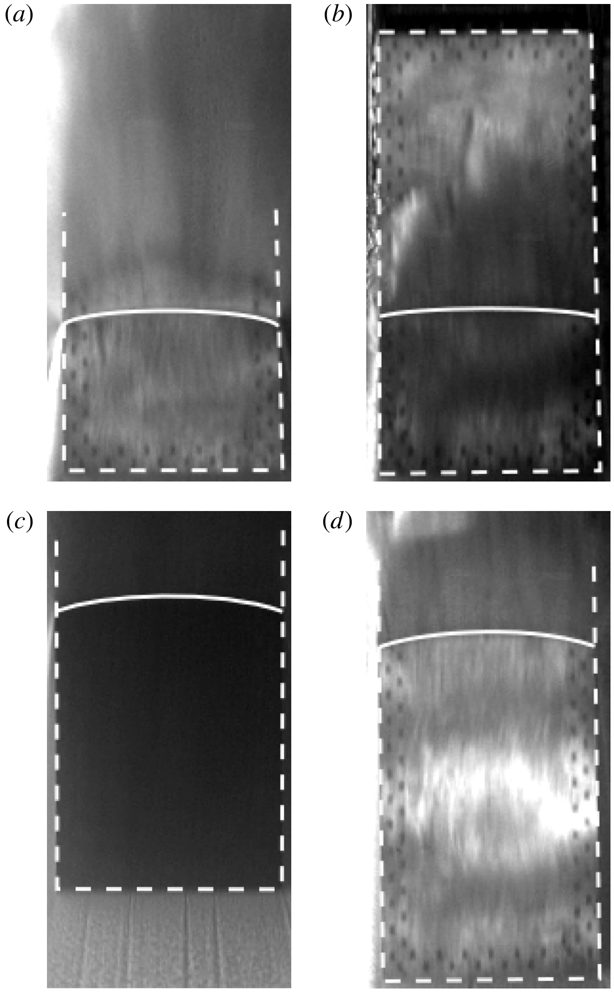

FIGURE 14. Underwater images of the tests at 10° (*a*,*c*) and 4° (*b*,*d*). The dashed lines are drawn around the edges of the plate. The trailing edge is in the lower part of the images and the plate is moving upwards. The white solid lines highlight the spray root. The images in (*a*,*b*) refer to a time T1 when the spray root is at sensor row *r*2, i.e. 0.40 m ahead of the trailing edge (figure 1). The images in (*c*,*d*) refer to a time T2 when the spray is approximately 0.65 and 0.80 m from the trailing edge for (*c*) and (*d*) respectively.

3.4. *Pressure distributions and scaling*

In Iafrati *et al.* (2015) some basic features of the pressure acting on the ditching plate have been discussed. In the following a more quantitative analysis of the data is presented, aimed at achieving a better comprehension of the role played by the different parameters.

The time histories of the pressure recorded during the tests at 40 and 45 m s^{-1} by probes located along the midline of the plate for the three different pitch angles are shown in figure 16. All of the curves are characterized by a quite similar behaviour: a sharp rise, a pressure peak and a gentle decay. Moreover, a widening of the area underneath the curves can be observed moving towards the leading edge of the plate.

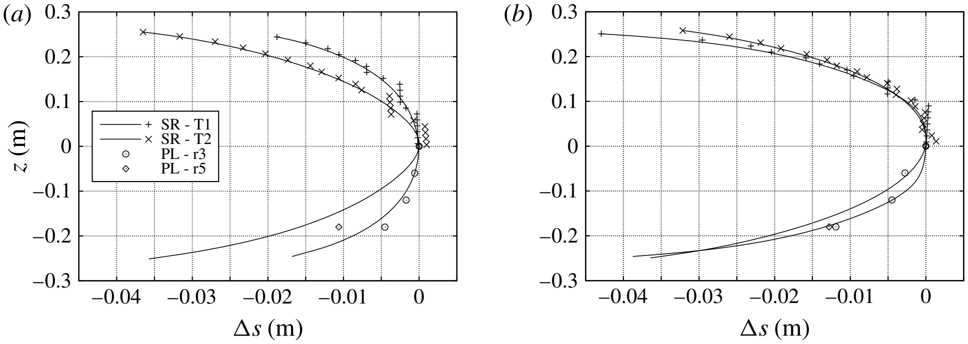

FIGURE 15. Comparison between the spray root (SR) derived from the underwater images in figure 14 and the data for the pressure peak lines (PL) provided in figure 13. For the sake of clarity, the symbols for the SR are shown for $z > 0$ only, whereas the symbols for $z \leqslant 0$ refer to the pressure peak lines. The data refer to the tests performed at 45 m s^{-1} for the 4° (*a*) and 10° (*b*) conditions.

Such features are consistent with the theoretical predictions discussed above. However, aside from some fluctuations, more evident at 4° due to the air cushion and to the bubble entrainment (Iafrati *et al.* 2015), the data display a general reduction of the pressure peak moving forward along the plate. As already discussed at the end of § 3.2, considering the increasing role played by the finiteness of the transverse dimension during the plate penetration and the changes in the pressure distribution observed in Battistin & Iafrati (2003) when passing from a cylinder to a sphere, such reduction in the pressure peak seems to be associated with three-dimensional effects.

It is worth noticing that the times of the sharp rises of the pressure in figure 16(*a*,*c*,*e*) and (*b*,*d*,*f*) are essentially the same. As observed when commenting on figure 7, this result indicates that the propagation along the plate is not greatly dependent on the horizontal velocity but rather on the vertical velocity and on the pitch angle, which, in the end, define the propagation velocity of the geometric intersection point.

The theoretical analysis presented in § 3.1 and, more specifically, the results in figure 4(*a*) have shown that the pressure peak equals the stagnation pressure associated with the horizontal velocity of the peak or, say, its absolute propagation velocity. Therefore, the reduction of the pressure peak observed in figure 16 moving forward along the plate might be simply explained by the reduction of the pressure peak propagation velocity (figure 8). In order to verify the above hypothesis, the coefficient

$$C_p^P = \frac{p^P}{\frac{1}{2}\rho(u_T + u_P)^2} \tag{3.6}$$

is computed for the pressure peaks p^P measured at the probes located along the midline of the plate in all test repeats, and results are reported in figure 17. On the basis of the positions of the probes given in figure 1, the data at $s = 0.125$ m refer to probe P4, those at $s = 0.25$ m to probe P8, and so forth, up to P18 at $s = 0.8$ m.

Aside from some scatter in the data, the results indicate that for all tests and for all probes the coefficient C_p^P is nearly one, confirming what has been discussed in § 3.1 for the theoretical solution. The origin of the scatter is in both the pressure peak and the propagation velocity. For the 4° case, and for P4 in particular, it is mainly related to the scatter in the pressure peak as a consequence of the air-cushion effect

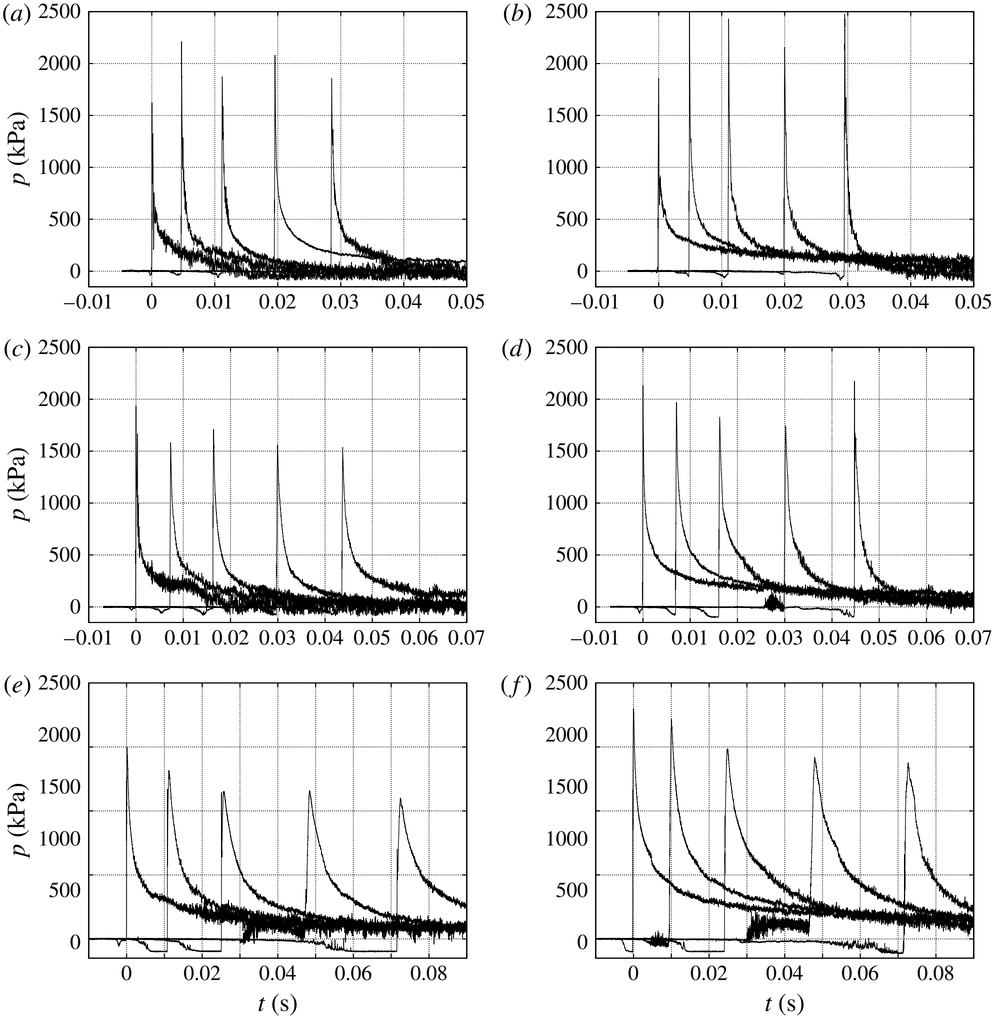

FIGURE 16. Time histories of the pressure measured by probes located along the midline of the plate during one single test performed at 40 m s^{-1} (*a*,*c*,*e*) and 45 m s^{-1} (*b*,*d*,*f*) horizontal velocity. In (*a*,*b*), (*c*,*d*) and (*e*,*f*) the data refer to 4°, 6° and 10° conditions respectively. Within each panel, the data from probes P4, P8, P12, P16 and P18 can be recognized by the position of the peak, which occurs earlier for probes located closer to the trailing edge.

and bubble entrainment (Iafrati *et al.* 2015). This also explains why the coefficient is greatly below one in some test repeats. In the 10° case, the close-up view of the pressure peak region provided in figure 18(*a*) displays a very good overlapping of the data for the 10 repeats carried out for the test condition at 40 m s^{-1}. The maximum variation of the pressure peak is of the order of 7 %, whereas the scatter in the C_p^P coefficient is of the order of 20 %. Hence, it is conjectured here that the additional variation is associated with the scatter in the propagation velocity observed in figure 10(*a*,*b*) for $t = 0$ s.

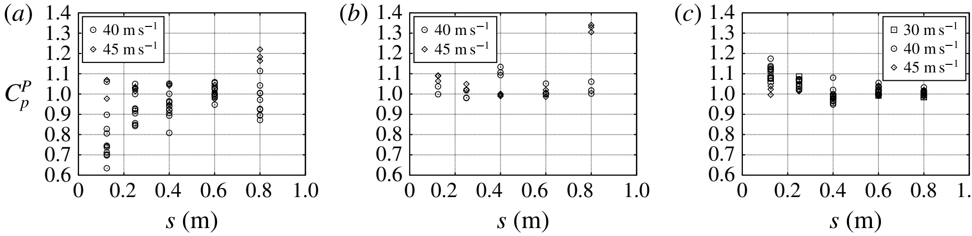

FIGURE 17. Pressure coefficients computed as in (3.6). From (*a*–*c*) the data refer to tests at 4°, 6° and 10° respectively. All repeats carried out at the same test conditions are shown.

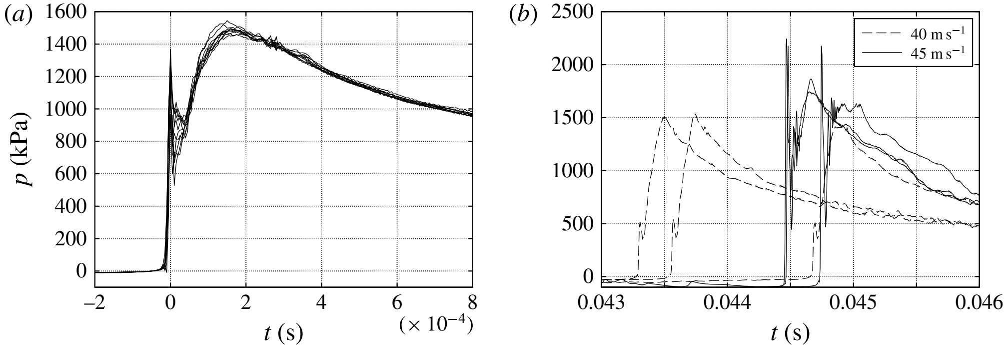

FIGURE 18. Close-up views of pressure peaks. (*a*) The pressure peak recorded at probe P4 in the 10 repeats of the tests at 10°, 40 m s^{-1} conditions. (*b*) A comparison of the pressure peaks measured at P18 during the three repeats of the tests at 6° for the 40 and 45 m s^{-1} conditions.

Some considerations are deserved by the double peak occurring in figure 18(*a*), the one on the left being quite sharp. The origin of the double peak in the pressure measurements is discussed in Iafrati *et al.* (2015), where it is shown that it is related to the interaction between the flow and the probe. This spurious first peak is responsible for the quite large pressures, with $C_p^P \simeq 1.3$, observed in the tests at 45 m s^{-1} and 6° (figure 17*b*). The close-up view of the pressure peak region for probe P18, displayed in figure 18(*b*), shows that at 45 m s^{-1} the first peak is much higher than that occurring at 40 m s^{-1}. This difference can be explained by the fact that the probes were removed and reinstalled between the two test series. It is believed that the differences in the first peak are related to the different positioning of the probe with respect to the plate surface. Nevertheless, these effects are characterized by a very short duration and have no influence on the next phase.

As said above, the fact that the pressure peak equals the stagnation pressure associated with its propagation velocity in the horizontal direction is indeed in agreement with the theory. However, since the propagation velocity is far below the theoretical value, the pressure peak intensity is correspondingly much lower than the value predicted by the self-similar solution. From table 2, for the 10° and $V/U = 0.0375$ conditions, the non-dimensional value of the pressure peak is $\psi^M = 1.261$, which corresponds to a peak value of approximately 2020 kPa. From figure 18(*a*) it is seen that at the probe P4, which is in the first sensor row where the propagation velocity has the maximum values among those observed along

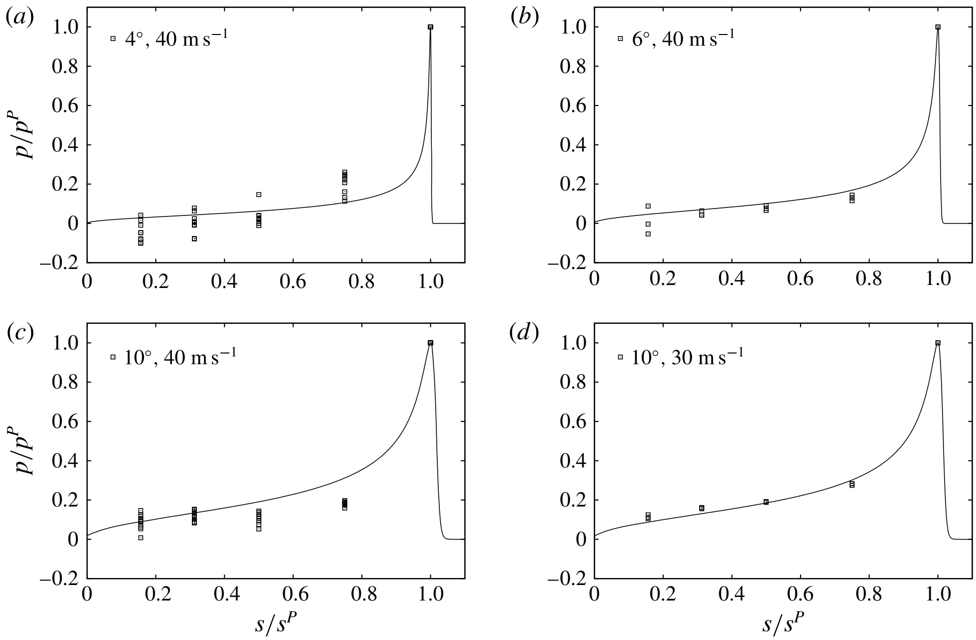

FIGURE 19. Pressure distributions: pressures measured in all test repeats by the probes located along the midline of the plate at the time when the peak arrives at P18. The horizontal and vertical axes are scaled by the abscissa (s^P) and intensity (p^P) of the pressure peak. The solid line represents the fully nonlinear self-similar theoretical solution.

the plate, the pressure peak is in a range between 1450 and 1550 kPa, far below the theoretical estimate. Moving forward along the plate, with the reduction of the propagation velocity the agreement is even worse, and at probe P18 the pressure peak drops to a range between 1080 and 1124 kPa.

The relations between the pressure peak and its propagation velocity or the propagation velocity of the geometric intersection point were already considered in Smiley (1951). As shown in figure 5 of Smiley (1951), for most of the data for the tests at pitch angle lower than 12° the pressure coefficients were far below one, which is apparently in contrast to the present data and to the classical results on water entry (Cointe & Armand 1987). It is believed that the too low sampling frequency and maybe the large size of the probes filtered the peak out (Van Nuffel *et al.* 2013).

Besides the pressure peak, it is interesting to establish comparisons in terms of the pressure distributions. A few points of the pressure profiles can be extracted from the time histories of the pressures measured by the five probes located at the middle of the plate at the time when the pressure peak is at P18. The data for tests performed at 40 m s^{-1} horizontal velocity, which correspond to $V/U = 0.0375$, for 4°, 6° and 10° pitch angle are shown in figure 19. For the 10° case the results at 30 m s^{-1}, or $V/U = 0.05$, are shown as well. The pressure values are scaled by the pressure peak measured at P18 and by its abscissa, $s^{18} = 0.800$ m.

As a general comment, the experimental data exhibit a drop on the left of the peak which is, on average, not far from the theoretical prediction. A quite good agreement is found for tests at 40 m s^{-1}, 6° and at 30 m s^{-1}, 10°. For the two tests at 40 m s^{-1}, 4° and 10°, the data at probe P16 are far above and far below the theoretical prediction respectively. With regard to the differences between the tests at 10° performed at 40

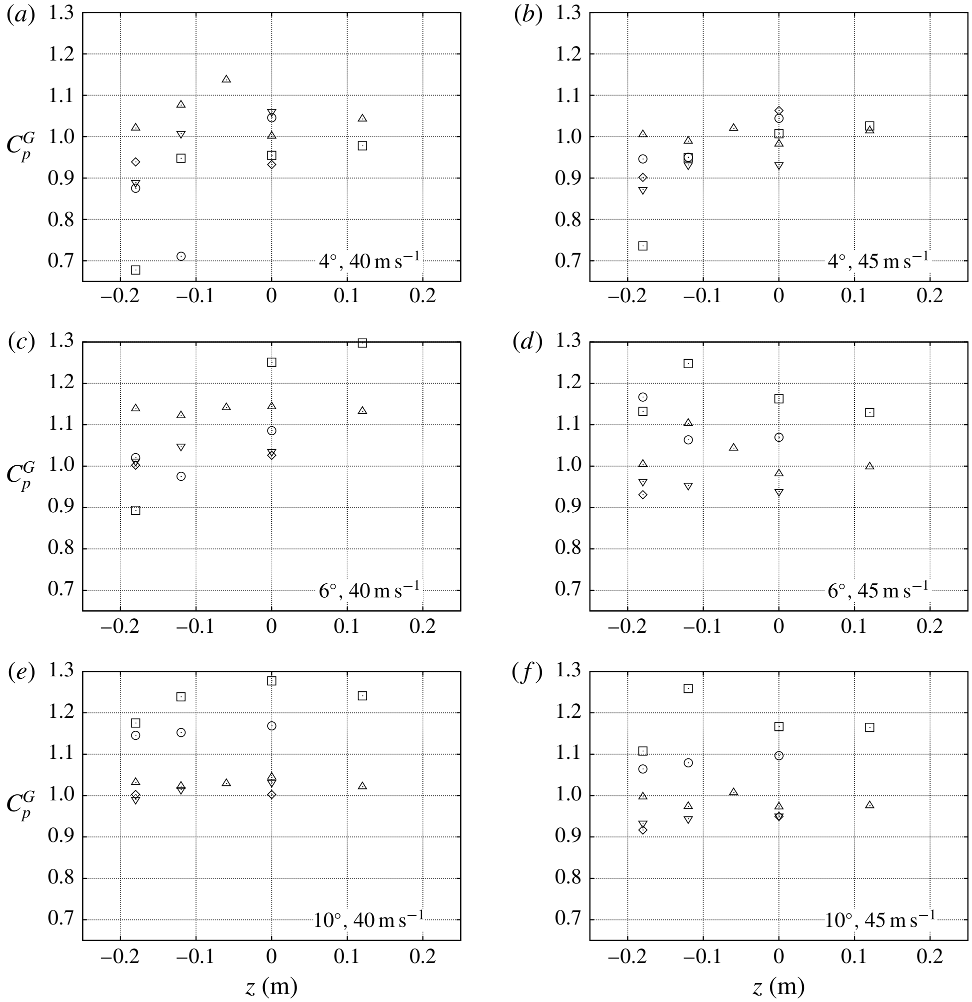

FIGURE 20. The transverse distribution of the pressure peaks at the different sensor rows: $r1$ (□), $r2$ (○), $r3$ (△), $r4$ (▽), $r5$ (◇).

and 30 m s^{-1}, it is not clear whether they are due to a different role played by the three-dimensional effects at 30 and 40 m s^{-1} or to the different bending of the guide.

In order to examine the role played by the sides and the effect of the flow in the transverse direction, the pressure peaks measured by the probes in different test conditions are drawn in figure 20 versus the transverse coordinate. The data are provided in terms of the ensemble averages over the repeats carried out in the same test conditions. It should be noted that, due some technical problems with the probe, the data for P3 are missing (Iafrati *et al.* 2015). Moreover, due to the problem with the first peak discussed above, the data for P18 are not reported for the test case at 6° and 45 m s^{-1}. As the propagation velocity is not available at all probes, the pressure coefficient is computed on the basis of the horizontal velocity of the geometric intersection point, that is

$$C_p^G = \frac{p}{\frac{1}{2}\rho(u_T + u_G^a)^2}. \tag{3.7}$$

In general, the data in figure 20 are characterized by quite large variations, which have different origins. For the 4° case, the variation is primarily related to the effect of the bubble entrainment and to the air cushion. Indeed, the pressure peaks recorded at the first row are far below those measured at the other rows. Moving forward, the pressure peaks rise and approach $C_p^G \simeq 1$, which is consistent with the values $u_P/u_G \simeq 1$ found at sensor row $r5$ (figure 8). For the test at 10°, the highest peaks are measured at the first row, and they gradually diminish moving forward. In this case the variation is only related to the reduction of the pressure peak propagation velocity.

Maybe because of the effects of the air cushion, for the 4° and 6° cases it is not possible to identify a clear dependence of the pressure peak on the transverse z-coordinate. For instance, in figure 20(*a*) the profile at row $r4$ display a maximum in the middle and a minimum at the side, but at row $r5$ probes P17 and P18 take approximately the same peak value. For the 10° case the transverse profiles are more regular. However, although the data at row $r1$ in figure 20(*e*) would suggest a distribution with the maximum at the middle, the profiles at the next sensor rows become more uniform. A nearly uniform distribution is also found in figure 20(*f*) for the tests at 45 m s^{-1}.

From the above considerations, it follows that the available data do not allow any conclusions to be derived on the side effect, which is in contrast with what is shown in figure 6(*a*,*b*) of Smiley (1951), where transverse distributions with peaks located a short distance from the edges appear for the 6° and 15° cases. Such a distribution is indeed consistent with what would be obtained by applying a $2D + t$ representation based on the pressure distribution generated during the water entry of a flat plate (Iafrati & Korobkin 2008). However, it seems that the profiles proposed in Smiley (1951) are rather fortuitous as they are based on a single test measurement and on the data from a single sensor row with four probes. According to what is shown in Iafrati & Korobkin (2008), the peak in the transverse distribution moves inwards as the plate penetrates, and thus it appears coincidental that the peak occurs at the same probe for 6° and 15°, also taking into account the different velocity reductions that characterize the two tests.

Nonetheless, a deeper investigation of the transverse distribution would be interesting. In particular, it would be important to understand to what extent the transverse distribution is affected by the differences in the set-up and in the test conditions adopted in the present experiments and in Smiley (1951). Among the most relevant differences, it is worth mentioning the aspect ratio of the plate and the corresponding three-dimensionality of the flow, the probe size and sampling rate and the variation of the entry velocity during the tests. Considering the quite high complexity of the test campaign, it is believed that such an investigation can only be conducted by using highly resolved numerical simulations of the three-dimensional problem.

3.5. *Hydrodynamic loads and scaling*

The loads acting on the plate are measured by a total of six piezoelectric cells, four used to measure the normal loads and two to measure the loads acting parallel to the plate, in the longitudinal direction. The latter are not relevant during the impact phase, that is the phase during which the spray root is propagating along the plate, even though they become quite large in the next phase when the leading edge of the plate falls below the still water level and help to stop the trolley before it reaches the end of the guide (Iafrati *et al.* 2015). For the purpose of the present study the normal loads are far more interesting and deserve consideration.

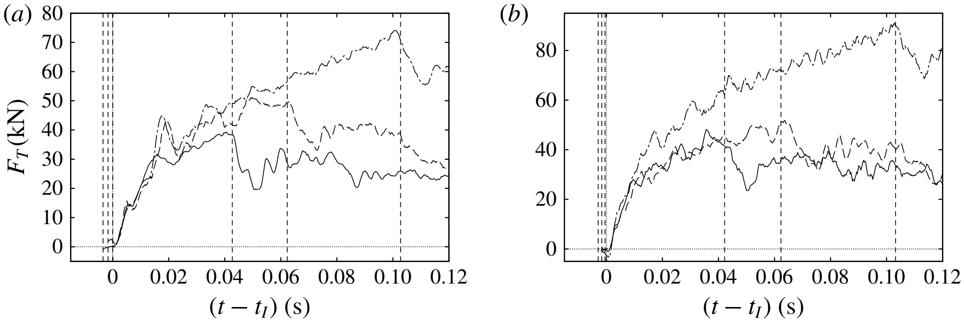

FIGURE 21. Comparison between the time histories of the normal loads measured in tests at 40 m s^{-1} (*a*) and 45 m s^{-1} (*b*) at 4° (solid), 6° (dashed) and 10° (dash–dot).

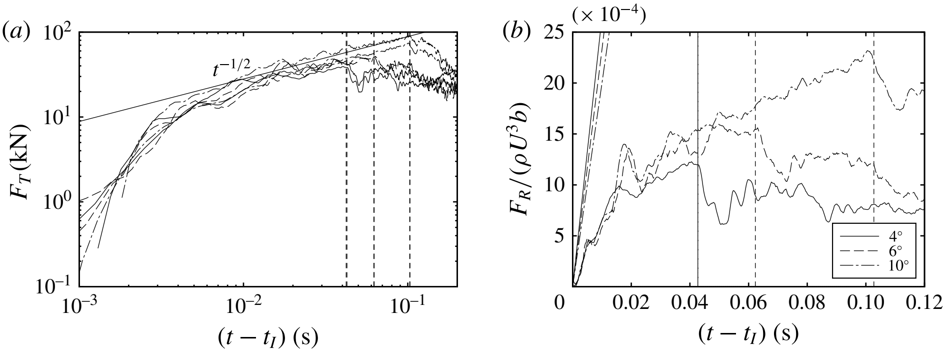

FIGURE 22. (*a*) The time histories of the normal loads measured at the three pitch angles and at the two horizontal speeds. All of the curves approach a $(t-t_I)^{1/2}$ behaviour for $t-t_I > 0.01$ s. (*b*) The normal loads measured in the tests at 40 m s^{-1} scaled as indicated in (3.3) and compared with the linear trend predicted by the self-similar two-dimensional model.

A preliminary analysis of the loads acting on the plates for the tests at 40 m s^{-1}, 4° and 10° pitch angles is presented in Iafrati *et al.* (2015), where the ensemble averages and the standard deviation of the data are provided. The normal loads measured in the different test conditions considered here are shown in figure 21. For each test condition the data are given in terms of the ensemble averages over the different repeats, and a time shift t_I is applied in order to have them synchronized at the initial contact. In all cases, soon after the initial contact, the data display a quasi-linear rise lasting a short time interval. Subsequently, the loads continue to increase but the growth rate diminishes. A sharp change in the slope occurs at approximately t–$t_I \simeq 0.01$ s, for all test conditions. The fact that the change in the slope is independent of the horizontal velocity and the pitch angle indicates that it is related to the penetration depth, the vertical velocity being the same for all test conditions.

The data show that for both the 40 and 45 m s^{-1} test conditions the curves display a quite similar initial trend and the slope in the next phase is also comparable. The differences in the maximum loads at the end of the entry process are a consequence of the different pitch angle, as shown later on. For a better estimate of the growth rate, the time histories of the normal loads are drawn in logarithmic scale in figure 22(*a*), and it is seen that for $t > 0.006$ s all curves approach a $t^{1/2}$ behaviour.

The above results differ considerably from the theoretical predictions. Of course, the theory predicts a linear variation, in contrast to the square-root variation exhibited by the measurements in the later stage of the water entry. Moreover, according to the data in table 2, the fully nonlinear model predicts a substantial dependence of the force coefficient on the pitch angle, the values for 6° and 4° being approximately 15 % and 30 % larger than that at 10° respectively, which is not observed in the experimental measurements. More relevant, however, is that the experimental data are far below the theoretical estimates. This is clearly shown in figure 22(*b*), where the forces measured in the tests at 40 m s^{-1} are scaled as in (3.3) and comparisons with corresponding linear trends based on the force coefficients $\mathscr{F}$ provided in table 2 are established. Quantitatively, for the 40 m s^{-1}, 10° conditions, the force coefficient provided by the theoretical model is 0.200. For a plate breadth of 0.5 m, from (3.3) 128 kN is obtained at $t - t_I = 0.02$ s, three times larger than the measured value of approximately 40 kN.

As the difference appears from the very beginning, it seems to be associated, mostly at least, with three-dimensional effects. In the previous sections reference has been already made to the comparison of the pressure distributions for a cylinder and a sphere provided in Battistin & Iafrati (2003). The results provided therein clearly show the substantial reduction of the pressure and of the wetted area, both effects contributing to a reduction of the loads occurring when the flow changes from a pure two-dimensional case to a pure three-dimensional one, which is what happens here in the first half of the entry phase. There could be, of course, some other effects related to the deceleration of the trolley or to the structural deformations of the guide, but they seem to be minor as the loads behave similarly in all test conditions (figure 22*a*).

The uncertainty in the data and the small changes in the values recorded for the different test conditions make the identification of a parametric dependence of the loads rather challenging. Furthermore, the comparison in terms of time histories is not fair as it is established among loads acting on different surface portions. On the basis of the data available from the experiments, there are two possible ways of comparing loads acting on the same surface. One way is to compare the loads at the time when the pressure peak arrives at the same sensor row. This approach is rather accurate, but it provides the data on five points only. Another option is to use the position of the geometric intersection point to retrieve the wetted length. Of course, such an approach is inherently approximate as the pressure peak propagation velocity is generally faster (figure 10), but it gives information also for the phase when the spray root is beyond sensor row *r*5, which is the phase when the highest loads are generated. For the purpose of the study, the latter approach is preferred. The time axis is multiplied by $V/\sin\alpha$, which is the velocity at which the geometric intersection point moves along the plate.

Results reported in figure 23(*a*,*b*) show that in all cases the lines at which the pressure peak arrives at the leading edge are located at approximately 0.9 m, and not at 1 m as they should be. This is of course a consequence of the assumption made about the propagation velocity, and confirms that, at least in the early phase, the pressure peak propagates faster than the geometric intersection point. Aside from such mismatch between the computed and the actual wetted surface, the representation in terms of the geometric wetted length clearly highlights the increase of the loads acting on the plate for larger pitch angles α, as a consequence of the higher value of the normal velocity component (3.5). This is confirmed by the data drawn in figure 23(*c*,*d*), where the loads are scaled by the square of the normal velocity component, U_n^2.

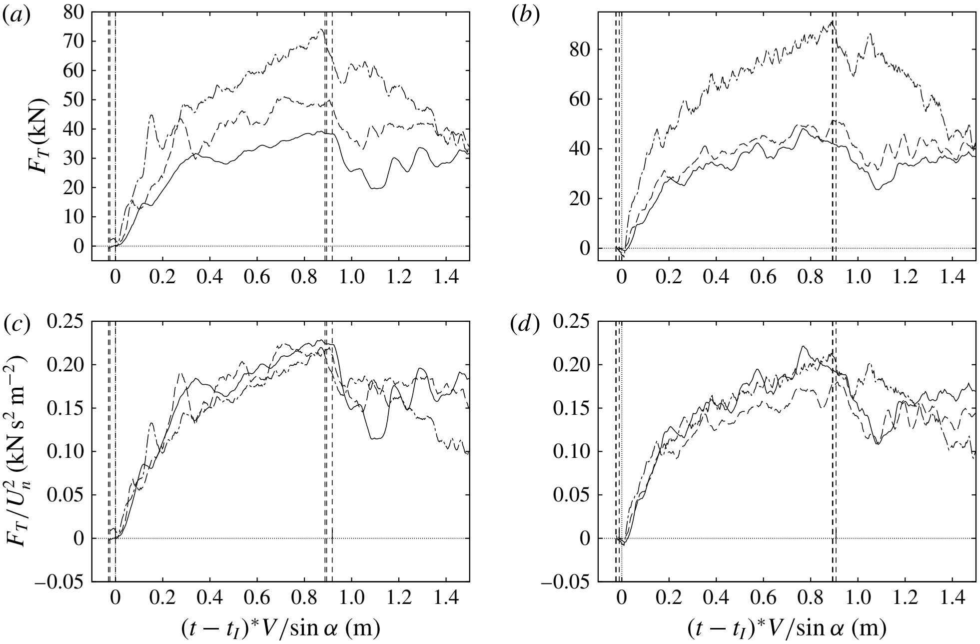

FIGURE 23. The loads acting on the plates as a function of the submerged length. The data refer to tests at 40 m s^{-1} (a,c) and 45 m s^{-1} (b,d) at 4° (solid), 6° (dashed) and 10° (dash–dot).

In order to distinguish the role played by the velocity from that of the pitch angle and guide inclination, a comparison is established in figure 24 between tests performed at different horizontal velocities but at the same α and β. As the measurements of single repeats are used for the tests at 34.5 and 38.5 m s^{-1}, the corresponding data are characterized by larger oscillations compared with those exhibited in the 40 m s^{-1} case for which the ensemble average is shown. However, on average, the three curves of the loads scaled by the square of the normal velocity exhibit a quite good overlapping. Since the two angles α and β are the same for the three tests, the results indicate that the loads scale with the square of the impact velocity.

Nevertheless, by comparing the results in figures 21(a) and 21(b) it is seen that the effect of the horizontal velocity is more relevant for large pitch angles because of the larger contribution to the normal velocity. This is made clearer in figure 25, where the loads measured during the tests performed at three different horizontal velocities but at the same vertical velocity and pitch angle are compared. Due to the large pitch angle, the loads display a large variation with the horizontal velocity. The data scaled by the square of the normal velocity exhibit a quite good overlapping, at least up to approximately half of the plate. Further, the data measured in the 30 m s^{-1} condition are somewhat beneath the other two solutions.

On the basis of the above considerations, it can be concluded that the parameters of the problem, i.e. horizontal velocity, vertical to horizontal velocity ratio and pitch angle, affect the loads mainly through their effect on the normal velocity component. Moreover, the results indicate that the pressure peak, being rather sharp, has only a limited effect on the loads.

Before closing the section, it is worth providing some data on the position of the centre of the loads s_c, which can be retrieved by exploiting the loads measured by the

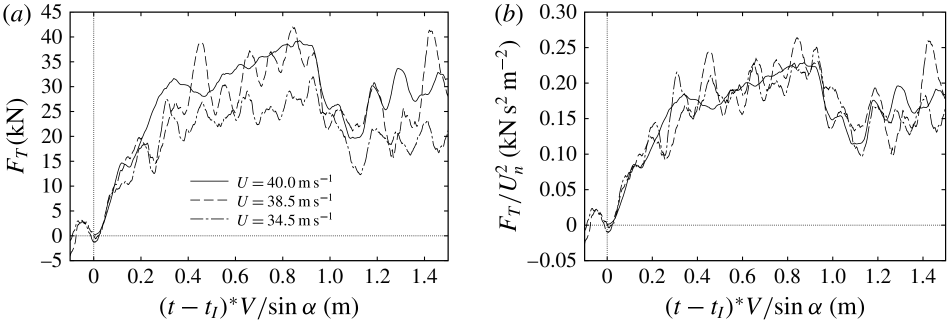

FIGURE 24. Comparison between loads measured during tests performed at different velocities, keeping the pitch angle (4°) and the inclination of the guide (1.5/40) constant.

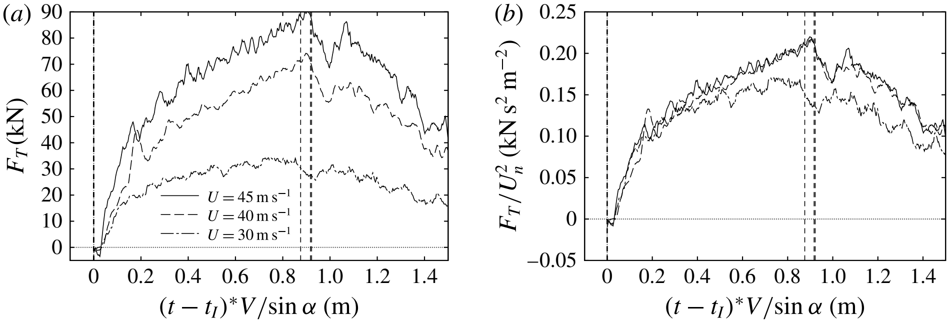

FIGURE 25. Comparison between loads measured during the tests at different horizontal velocities and guide inclinations, keeping the pitch angle (10°) and the vertical velocity ($V = 1.5$ m s^{-1}) constant.

two couples of load cells located at the rear and ahead of the box structure carrying the plates (Iafrati *et al.* 2015). The data for the three pitch angles and different horizontal velocities are shown in figure 26, together with the lines that identify the time of initial contact and that at which the pressure peak reaches the leading edge. In the very early stage, the loads measured by the cells are of small amplitude and the oscillations are such that unrealistic locations of the centre of the loads are obtained. These values are not shown in the graphs. In all cases, the coordinate s_c is characterized by a sharp initial growth up to $t \simeq 0.01$ s and follows a linear rise afterwards. The data indicate that there is no significant effect of the horizontal velocity. It is interesting to note that in all cases the maximum value is taken at the time when the pressure peak reaches the leading edge, when $s_c \simeq 0.8$ m. In the next stage, the pressure peak leaves the plate surface and the pressure is more uniform along the plate, which is the reason why the centre of the loads moves backwards.

4. Concluding remarks

An experimental investigation of the water entry of a rectangular plate with a high horizontal velocity component has been presented. Three main parameters have been considered: horizontal velocity, vertical to horizontal velocity ratio and pitch angle. The analysis of the data has been focused on the spray formation, spray root shape,

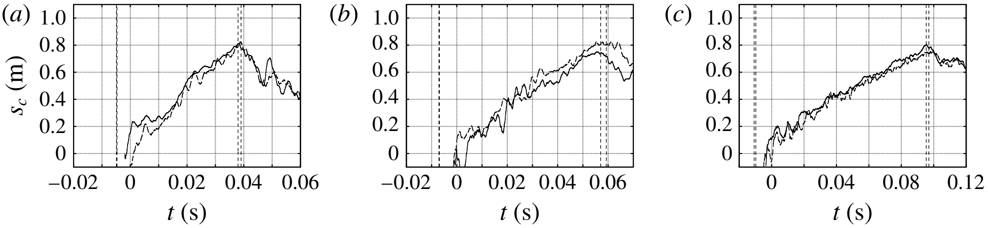

FIGURE 26. Time histories of the centre of the loads for the tests at 40 m s^{-1} (solid) and 45 m s^{-1} (dashed). From (*a–c*) the data refer to tests at 4°, 6° and 10° respectively.

pressure distribution and scaling, pressure peak and propagation velocity, total loads acting on the plates and position of the centre of the loads.

It has been shown that at the beginning of the water entry process the propagation velocity of the pressure peak is higher than that of the geometric intersection between the undisturbed free surface and the plate. However, this stage only lasts for a short time interval. As the plate penetrates, the third dimension becomes more important and there is an increased possibility for the fluid to move towards the sides. The propagation velocity of the pressure peak diminishes and at the end of the entry process it approaches that of the geometric intersection point.

The transverse shape of the pressure peak line has been retrieved from the pressure measurements by computing the times at which the pressure peak crosses the different probes. Hence, the propagation velocity of the pressure peak is used to transform the time delays into distances. Some comparisons with the spray root shape derived from underwater images have been also established, achieving a quite satisfactory agreement. It has been found that, in a late stage of the entry process, the spray root curvature is the same for all test conditions, but at lower pitch angles, due to the reduced three-dimensional effects, the curvature displays a more gradual growth.

Except for a reduced number of cases in which the air cushion causes a reduction in the pressure, it has been confirmed that the pressure peak intensity equals the stagnation pressure of the corresponding propagation velocity in the horizontal plane. Nevertheless, it has been seen that the pressure peak is not very relevant as far as the total loads are concerned. The loads are found to be more dependent on the stagnation pressure associated with the normal velocity acting on the plate.

It is worth remarking that no data have been presented here in terms of the structural deformation of the plate. This is because, due to the large thickness of the plate, the structural deformations were found to be rather small and had no effects on the hydrodynamic aspects investigated here. Some more information about the structural deformations measured in the tests is provided in Iafrati *et al.* (2015), whereas a preliminary study of the effects of large structural deformations experienced by thin plates on the hydrodynamics is addressed in Iafrati (2015) and will be the subject of future studies.

Acknowledgements

This work was carried out in the framework of the SMAES-FP7 project (grant agreement no. 266172). The activities were partially funded by the Flagship Project RITMARE – The Italian Research for the Sea – coordinated by the Italian National Research Council and funded by the Italian Ministry of Education, University and

Research within the National Research Program 2014–2015. The author thanks K. J. Maki and M. Siemann for some helpful discussions during the preparation of the manuscript.

Appendix A. Fully nonlinear model

By assuming the plate to be infinitely long, the two-dimensional water entry flow with horizontal velocity can be studied with the hypothesis of self-similarity under the set of variables (3.1). In this condition, the initial boundary value problem governing the solution is transformed into a boundary value problem. The velocity potential satisfies the Laplace equation

$$\nabla^2\varphi = 0 \tag{A 1}$$

in the fluid domain Ω. The normal velocity is assigned on the plate surface as

$$\varphi_n = \sin\alpha + \frac{V}{U}\cos\alpha, \quad \eta = -\frac{V}{U} + (\xi - 1)\tan\alpha, \tag{A 2a,b}$$

where α is the pitch angle, n is the unit normal to the boundary, oriented towards the fluid domain, and subscripts denote partial derivatives with respect to the variable. In terms of the new variables, the kinematic and dynamic boundary conditions

$$-(\xi h_\xi + \eta h_\eta) + (h_\xi\varphi_\xi + h_\eta\varphi_\eta) = 0, \quad h(\xi,\eta) = 0, \tag{A 3}$$

$$\varphi - (\xi\varphi_\xi + \eta\varphi_\eta) + \tfrac{1}{2}\left(\varphi_\xi^2 + \varphi_\eta^2\right) = 0, \quad h(\xi,\eta) = 0 \tag{A 4}$$

have to be satisfied on the free surface, which is represented by the equation $h(\xi,\eta) = 0$. Finally, it is assumed that the free surface is attached at the leading edge and leaves the plate tangentially, i.e.

$$h(1, -V/U) = 0, \quad h_\xi(1, -V/U) = \tan\alpha. \tag{A 5a,b}$$

For the solution of the boundary value problem, a modified velocity potential $S = \varphi - (\xi^2 + \eta^2)/2$ is introduced to simplify the kinematic and dynamic boundary conditions, which become

$$S_n = 0, \quad S_\varsigma = \pm\sqrt{-2S} \tag{A 6a,b}$$

respectively, where ς is the abscissa along the free surface. It can be shown that the sign in the dynamic boundary condition is always negative on the right-hand side, whereas it changes along the free-surface portion behind the trailing edge. The sign is positive just behind the trailing edge, changes at the inversion point (ξ_I, η_I) (see figure 2) and takes a negative sign as $\xi \to -\infty$. By following the approach used in Iafrati & Korobkin (2004), the position of the inversion point is derived as part of the solution by enforcing the Kutta conditions (A 5).

The solution inside the thin jet layer is computed by a shallow water model, as discussed in Iafrati & Korobkin (2004) and adopted for a similar flow configuration in Battistin & Iafrati (2004). The boundary value problem is solved iteratively until convergence on the main parameters is achieved.

The distribution of the non-dimensional pressure (3.2) is derived from the self-similar velocity potential as

$$\psi(\xi,\eta) = -\varphi + (\xi\varphi_\xi + \eta\varphi_\eta) - \tfrac{1}{2}(\varphi_\xi^2 + \varphi_\eta^2). \tag{A 7}$$

Integration of (A 7) along the wetted portion of the plate provides the hydrodynamic load in non-dimensional form (3.3) as

$$\mathscr{F} = \int_0^{\sigma_T} \psi(\xi(\sigma), \eta(\sigma))\,\mathrm{d}\sigma, \tag{A 8}$$

where σ is the abscissa along the body surface with origin at the trailing edge of the plate and σ_T is the abscissa at the spray tip (figure 2).

REFERENCES

BATTISTIN, D. & IAFRATI, A. 2003 Hydrodynamic loads during water entry of two-dimensional and axisymmetric bodies. *J. Fluids Struct.* **17**, 643–664.

BATTISTIN, D. & IAFRATI, A. 2004 A numerical model for the jet flow generated by water impact. *J. Engng Maths* **48**, 353–374.

BRENNEN, C. E. 2005 *Fundamentals of Multiphase Flow*. Cambridge University Press.

CHUANG, S. L. 1967 Experiments on slamming of wedge-shaped bodies. *J. Ship. Res.* **11**, 190–198.

CLIMENT, H., BENITEZ, L., ROSICH, F., RUEDA, F. & PENTECOTE, N. 2006 Aircraft ditching numerical simulation. In *Proceedings of the 25th International Congress of the Aeronautical Sciences, 3–8 September 2006, Hamburg, Germany*.

COINTE, R. & ARMAND, J.-L. 1987 Hydrodynamic impact analysis of a cylinder. *J. Offshore Mech. Arctic. Engng* **109**, 237–243.

FALTINSEN, O. M. & SEMENOV, Y. A. 2008 Nonlinear problem of flat-plate entry into an incompressible liquid. *J. Fluid Mech.* **611**, 151–173.

GUO, B., LIU, P., QU, Q. & WANG, J. 2013 Effect of pitch angle on initial stage of a transport airplane ditching. *Chinese J. Aeronaut.* **26**, 17–26.

HOWISON, S. D., OCKENDON, J. R. & WILSON, S. K. 1991 Incompressible water-entry problems at small deadrise angles. *J. Fluid Mech.* **222**, 215–230.

IAFRATI, A. 2015 Fluid–structure interactions during the high speed water entry of a plate. In *Proceedings of the 18th International Conference on Ships and Shipping Research, 24–26 June 2015, Lecco, Italy*.

IAFRATI, A. & BATTISTIN, D. 2003 Hydrodynamics of water entry in presence of flow separation from chines. In *Proceedings of the 8th International Conference on Numerical Ship Hydrodynamics, 22–25 September 2003, Busan, Korea*.

IAFRATI, A. & CALCAGNI, D. 2013 Numerical and experimental studies of plate ditching. In *Proceedings of the 28th International Workshop Water Waves Floating Bodies, 7–10 April 2013, Marseille, France*, available online at www.iwwwfb.org.

IAFRATI, A., GRIZZI, S., SIEMANN, M. & BENÍTEZ MONTAÑÉS, L. 2015 High-speed ditching of a flat plate: experimental data and uncertainty assessment. *J. Fluids Struct.* **55**, 501–525.

IAFRATI, A. & KOROBKIN, A. 2004 Initial stage of flat plate impact onto liquid free surface. *Phys. Fluids* **16**, 2214–2227.

IAFRATI, A. & KOROBKIN, A. 2008 Hydrodynamic loads during early stage of flat plate impact onto water surface. *Phys. Fluids* **20**, 082104.

KAPSENBERG, G. K. 2011 Slamming of ships: where are we now? *Phil. Trans. R. Soc. Lond.* A **369**, 2892–2919.

KOROBKIN, A. A. & PUKHNACHOV, V. V. 1988 Initial stage of water impact. *Annu. Rev. Fluid Mech.* **20**, 159–185.

KOROBKIN, A. A. & SCOLAN, Y.-M. 2006 Three-dimensional theory of water impact. Part 2. Linearized Wagner problem. *J. Fluid Mech.* **549**, 343–373.

MCBRIDE, E. E. & FISHER, L. J. 1953 Experimental investigation of the effect of rear-fuselage shape on ditching behavior. *Tech. Note* 2929. National Advisory Council for Aeronautics (NACA), Langley Field, VA, USA.

MOGHISI, M. & SQUIRE, P. T. 1981 An experimental investigation of the initial force of impact on a sphere striking a liquid surface. *J. Fluid Mech.* **108**, 133–146.

OKADA, S. & SUMI, Y. 2000 On the water impact and elastic response of a flat plate at small impact angles. *J. Mar. Sci. Technol.* **5**, 31–39.

REINHARD, M., KOROBKIN, A. A. & COOKER, M. J. 2013 Water entry of a flat elastic plate at high horizontal speed. *J. Fluid Mech.* **724**, 123–153.

SEDDON, C. M. & MOATAMEDI, M. 2006 Review of water entry with applications to aerospace structures. *Intl J. Impact Engng* **32**, 1045–1067.

SEMENOV, YU. A. & IAFRATI, A. 2006 On the nonlinear water entry problem of asymmetric wedges. *J. Fluid Mech.* **547**, 231–256.

SIEMANN, M. H. & GROENENBOOM, P. H. L. 2014 Modeling and validation of guided ditching tests using a coupled SPH–FE approach. In *Proceedings of the 9th International SPHERIC Workshop, 3–5 June 2014, Paris, France*.

SIEMANN, M. H., KOHLGRUBER, D., BENÍTEZ MONTAÑÉS, L. & IAFRATI, A. 2014 Numerical simulation and experimental validation of guided ditching tests. In *Proceedings of the 11th World Congress on Computational Mechanics (WCCM XI), 20–25 July 2014, Barcelona, Spain*.

SMILEY, R. F. 1950 A study of water pressure distribution during landings with special reference to a prismatic model having a heavy beam loading and a 30° angle of dead rise. *Tech. Note* 2111, National Advisory Council for Aeronautics (NACA), Langley Field, VA, USA.

SMILEY, R. F. 1951 An experimental study of water-pressure distributions during landings and planing of a heavily loaded rectangular flat-plate model. *Tech. Note* 2453, National Advisory Council for Aeronautics (NACA), Langley Field, VA, USA.

SMILEY, R. F. 1952 A theoretical and experimental investigation of the effects of yaw on pressures, forces, and moments during seaplane landings and planing. *Tech. Note* 2817, National Advisory Council for Aeronautics (NACA), Langley Field, VA, USA.

SMITH, A. G., WARREN, C. H. E. & WRIGHT, D. F. 1957 Investigations of the behaviour of aircraft when making a forced landing on water (ditching). Reports and Memoranda 2917, Aeronautical Research Council, Ministry of Supply.

STENIUS, I., ROSÈN, A., BATTLEY, M. & ALLEN, T. 2013 Experimental hydroelastic characterization of slamming loaded marine panels. *Ocean Engng* **74**, 1–15.

STRECKWALL, H., LINDENAU, O. & BENSCH, L. 2007 Aircraft ditching: a free surface/free motion problem. *Arch. Civil Mech. Engng* **3**, 178–190.

VAN NUFFEL, D., VEPA, K. S., DE BAERE, I., DEGRIECK, J., DE ROUCK, J. & VAN PAEPEGEM, W. 2013 Study on the parameters influencing the accuracy and reproducibility of dynamic pressure measurements at the surface of a rigid body during water impact. *Exp. Mech.* **53**, 131–144.

ZHANG, T., LI, S. & DAI, H. 2012 The suction force effect analysis of large civil aircraft ditching. *Sci. China Technol. Sci.* **55**, 2789–2797.

ZHAO, R., FALTINSEN, O. M. & AARSNES, J. 1996 Water entry of arbitrary two-dimensional sections with and without flow separation. In *Proceedings of the 21st Symposium on Naval Hydrodynamics, 24–28 June 1996, Trondheim, Norway*.

ZHAO, R., FALTINSEN, O. M. & HASLUM, H. A. 1997 A simplified nonlinear analysis of a high-speed planing craft in calm water. In *Proceedings of the Fourth International Conference on Fast Sea Transportation, FAST'97, 21–23 July 1997, Sydney, Australia*.